Mert *et al. Earth, Planets and Space* (2016) 68:146
DOI 10.1186/s40623-016-0520-3

Earth, Planets and Space

FULL PAPER Open Access

Physically based probabilistic seismic hazard analysis using broadband ground motion simulation: a case study for the Prince Islands Fault, Marmara Sea

Aydin Mert[1*], Yasin M. Fahjan[2], Lawrence J. Hutchings[3] and Ali Pınar[1]

Abstract

The main motivation for this study was the impending occurrence of a catastrophic earthquake along the Prince Island Fault (PIF) in the Marmara Sea and the disaster risk around the Marmara region, especially in Istanbul. This study provides the results of a physically based probabilistic seismic hazard analysis (PSHA) methodology, using broadband strong ground motion simulations, for sites within the Marmara region, Turkey, that may be vulnerable to possible large earthquakes throughout the PIF segments in the Marmara Sea. The methodology is called physically based because it depends on the physical processes of earthquake rupture and wave propagation to simulate earthquake ground motion time histories. We included the effects of all considerable-magnitude earthquakes. To generate the high-frequency (0.5–20 Hz) part of the broadband earthquake simulation, real, small-magnitude earthquakes recorded by a local seismic array were used as empirical Green's functions. For the frequencies below 0.5 Hz, the simulations were obtained by using synthetic Green's functions, which are synthetic seismograms calculated by an explicit 2D/3D elastic finite difference wave propagation routine. By using a range of rupture scenarios for all considerable-magnitude earthquakes throughout the PIF segments, we produced a hazard calculation for frequencies of 0.1–20 Hz. The physically based PSHA used here followed the same procedure as conventional PSHA, except that conventional PSHA utilizes point sources or a series of point sources to represent earthquakes, and this approach utilizes the full rupture of earthquakes along faults. Furthermore, conventional PSHA predicts ground motion parameters by using empirical attenuation relationships, whereas this approach calculates synthetic seismograms for all magnitudes of earthquakes to obtain ground motion parameters. PSHA results were produced for 2, 10, and 50 % hazards for all sites studied in the Marmara region.

Keywords: Simulation of strong ground motion, Probabilistic seismic hazard assessment, Empirical Green's function, Synthetic Green's function, Prince Island Fault

Introduction

The Marmara region of northwest Turkey is located at the western end of the North Anatolian Fault Zone (NAFZ), a main strike-slip fault system that has produced remarkable sequences of destructive earthquakes throughout its length of more than 1500 km (Ambraseys and Finkel 1991; Ambraseys and Jackson 2000; Ambraseys 2002a, b) (Fig. 1). This strike-slip fault zone is a continuous and narrow fault system that cuts across the Anatolian Peninsula in the E–W direction from Karliova in the east to the northern Aegean in the west. Because the N–S extensional regime of the Aegean region and the NAFZ, as the northern plate boundary of the Anatolian Plate, intersect, contrary to the simple structure of the NAFZ along the entire fault zone, in the eastern part of the Marmara region, the NAFZ does not continue as a single fault line but rather spreads out as a complex fault system. It splits

*Correspondence: mertay@boun.edu.tr
[1] Department of Earthquake Engineering, Boğaziçi University Kandilli Observatory and Earthquake Research Institute, İstanbul, Turkey
Full list of author information is available at the end of the article

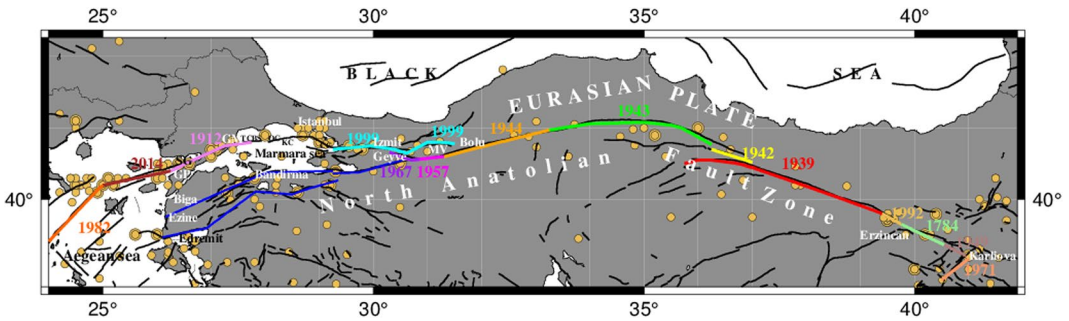

Fig. 1 The 1600-km-long NAFZ and the seismicity of Anatolia. The solid black lines portray the active faults given in Emre and Duman (2011). The colored solid lines show segmentations compiled from Armijo et al. (2002), Kurtuluş and Canbay (2007), Ustaomer et al. (2008), and Yilmaz et al. (2009). The epicenters indicate the locations of the historical and instrumental period earthquakes of magnitudes $M_w \geq 6.0$ compiled by Grünthal and Wahlström (2012) and Akkar et al. (2014). TC: Tekirdag Basin, BS: West Ridge, KC: Kumburgaz Basin, OC: Middle Marmara Basin, CC: Cinarcik Basin, MV: Mudurnu Valley, SG: Saros Gulf, GP: Gelibolu Peninsula, GM: Ganos Mountains)

into two main branches around Bolu, which are referred to as the Northern Splay and the Southern Splay (Fig. 1).

Offshore and onshore high-resolution seismic profiles (Carton et al. 2007; Laigle et al. 2008; Becel et al. 2009) and high-resolution bathymetry studies, including geological, geomechanical (Görür et al. 1997; Yilmaz et al. 2009; Hergert et al. 2011) and GPS studies (Ergintav et al. 2014), have been finalized recently in the Marmara region, and these reveal that the northern branch of the NAFZ, before entering the Marmara Sea, is observed as one continuous segment along Izmit Bay and at its entrance to the sea southeast of Istanbul. Current investigations have definitely confirmed that the majority of the long-term fault slip occurs along the offshore section of the northern fault segment following the northwest striking Prince Island Fault (PIF) combined with the east–west striking Central Marmara Fault (CMF) immediately south of Istanbul (Le Pichon et al. 2001; Armijo et al. 2005; Ergintav et al. 2014). Together with seismological and seismotectonic studies (Gürbüz et al. 2000; Oncel and Wyss 2001; Oncel and Wilson 2006; Kalafat et al. 2011), recent GPS and kinematic studies (Meade et al. 2002; Flerit et al. 2003) have indicated that the northern branch of the NAFZ is more active and also creates much larger motion than the southern branch. This hypothesis has also been verified by historical period (Ambraseys and Jackson 2000; Ambraseys 2001a, b, 2002a, b), instrumental period (Kalafat et al. 2011), and recent detailed microearthquake seismicity studies (Sato et al. 2004; Bohnhoof et al. 2013). The northern branch of the NAFZ in the Sea of Marmara, extending for more than 150 km, has been identified as a seismic gap because it has not generated a strong earthquake during the earthquake series of the last century (Bohnhoof et al. 2013). If we consider that the annual dextral motion across the Marmara Sea is 23–24 mm/year and that the last significant earthquake occurred in 1766, this seismic gap may have accumulated a slip deficit of more than 5 m (Bohnhoof et al. 2013).

During the twentieth century, the NAFZ experienced an exceptional seismic moment release cycle, which ruptured the entire fault zone and produced devastating earthquakes (1939 M_s 7.8, 1942 M_s 7.1, 1943 M_s 7.3, 1944 M_s 7.3, 1957 M_s 7.0, 1967 M_s 7.1, 1999 M_w 7.2, 1999 M_w 7.4), except at two segments (Fig. 1), one beneath the Marmara Sea and the other farther to the west beneath the northern Aegean Sea. The ruptures resulting from the 1999 Izmit and Duzce earthquakes represent the last series of the catastrophic earthquakes along the northern branch of the NAFZ (Stein et al. 1997; Nalbant et al. 1998; Toksöz et al. 1999) in the eastern part of the Marmara Sea. Another destructive earthquake occurred in the western part of the Marmara Sea in 1912 (Murefte–Sarkoy event) along the northern branch of the NAFZ. The 2014 event filled one of the aforementioned seismic gaps, leaving only the Marmara faults unruptured. The only branch of the NAFZ that has not generated destructive earthquakes during this century and the last century is the Marmara Sea segments (PIF and CMF) (Ergintav et al. 2014).

During the 60 years from 1939 to 1999 and from Erzincan to Izmit, the entire NAFZ was broken in a sequence of westward-propagating earthquakes (Stein et al. 1997). Because the likely post-seismic stress distribution was completely altered after the 1999 earthquake sequences, the offshore segment of the northern branch of the NAFZ is exposed to enhanced stresses (Parsons et al. 2000; Hubert-Ferrari et al. 2000; Pondard et al. 2007). According to Parsons (2004) who considered a time-dependent model in which the coseismic and post-seismic effects of the 1999 $M = 7.4$ Izmit earthquake were encountered, the probability of occurrence of an $M \geq 7$ earthquake

beneath the Sea of Marmara for the next 30 years after the 1999 Izmit and Düzce earthquakes was increased to 35–70 %.

Because of the increasing awareness of the threat of earthquake in the Marmara region, the significance of seismic hazard studies has become progressively more important, especially for earthquake risk reduction not only for the Istanbul metropolitan area but also for the entire Marmara region. The earthquake hazard in the Marmara region has been studied by probabilistic methods (Atakan et al. 2002; Erdik et al. 2004). In addition to these earthquake hazard assessment studies, some researchers have attempted to model bedrock ground motions in the Marmara region using the hybrid broadband simulation technique (Pulido et al. 2004; Sørensen et al. 2007, Ansal et al. 2009; Tanircan 2012; Mert et al. 2014a, b). Pulido et al. (2004) merged deterministic simulation for low-frequency ground motion with a semi-stochastic procedure forhigh-frequency ground motion in order to model broadband seismic wave propagation at bedrock in the Marmara region.

Sørensen et al. (2007) also used the same hybrid model semi-stochastic methodology to estimate high frequencies and a deterministic model for low frequencies to assess the effect of source and attenuation parameters on simulated ground motion. Ansal et al. (2009), to improve loss scenarios from earthquake, especially in terms of damage to buildings and casualties in Istanbul, calculated synthetic time series of ground motion using a methodology based on a hybrid stochastic–deterministic approach. Tanircan (2012), using a finite difference algorithm and combining it with a three-dimensional velocity structure for low-frequency and a stochastic algorithm for high-frequency earthquake simulation, obtained hybrid simulation of ground motion for Istanbul for three different scenarios as a result of an $M_w = 7.2$ earthquake on the PIF. Mert et al. (2014a, b) applied a hybrid strong ground motion simulation methodology for the PIF. By changing different earthquake source parameters, they investigated the parameters' effects on the amplitude and frequency contents of the synthetic ground motions. They used a finite difference algorithm to obtain synthetic Green's functions (SGFs) for the low-frequency part of the simulations and real recorded earthquakes as empirical Green's functions (EGFs) for the high-frequency part of the simulations and then obtained broadband simulations by using a physically based simulation method and an in-house merging algorithm.

Ergintav et al. (2014) used more than 20 years of GPS observations to evaluate strain accumulation along the northern branch of the NAFZ, namely the PIF and CMF. They reported that despite the CMF having been assumed by several researchers to be the most probable location for the next destructive earthquake within the Sea of Marmara the GPS data show no evidence of strain accumulation. They also claimed that a significant portion of the CMF is creeping and pointed out that the PIF is the most probable location of the next $M > 7$ earthquake along the seismic gap of the Marmara Sea.

The main motivation of this study is that the inevitability of the occurrence of such a destructive earthquake along the PIF in the Marmara Sea results in increased earthquake disaster risk around the Marmara region, especially in Istanbul. Historical earthquake catalogs including data through two millennia indicate that at least one medium-sized earthquake has affected the city of Istanbul every 50 years (Ambraseys and Finkel 1991). According to the same catalogs, the average return period of a catastrophic event is about 300 years (Durukal and Erdik 1994). Considering the facts that Istanbul accommodates about one-sixth of the total population of Turkey, one-half of its industrial potential, and produces at least 25 % of its GNP, the earthquake risk of Istanbul can be clearly understood. Other significant reasons of increased risk in Istanbul are a very high rate of suburbanization, environmental deterioration, and incorrect land use planning and architecture (Erdik et al. 2003). The goal of this study was to estimate a PSHA using broadband strong ground motion simulations within the Marmara region, Turkey, for possible earthquakes along the PIF segments in the Marmara Sea.

We utilized the broadband ground motion simulations to achieve a broadband PSHA for all considerable-magnitude earthquakes. This was the basis for identifying appropriate ground motions to use to calculate a dynamic analysis of the engineering structures and the earthquake response thus risk. The physically based PSHA used here followed the same procedure as conventional PSHA, except that conventional PSHA utilizes point sources or a series of point sources to represent earthquakes whereas this approach utilizes full rupture of earthquakes along faults. Furthermore, conventional PSHA predicts ground motion parameters by using empirical attenuation relationships, whereas this approach calculates synthetic seismograms for all magnitudes of earthquakes to obtain ground motion parameters. Based on these calculations, PSHA results were produced and presented for 2, 10, and 50 % hazards for all of sites studied in the Marmara region.

Methodology

To identify the rupture process of an earthquake, the ultimate solution would be dynamic solutions identified by elastic constants and constituent relations that satisfy the elastodynamic equation of seismology and fracture energy. On the other hand, these considerations are

generally unpredictable in the fault rupture area and several poorly bounded assumptions are required to identify them. In this study, we used a physically based methodology to investigate the range of ground motion hazard for earthquakes throughout particular faults and combined this methodology into PSHA. To perform PSHA for specific sites, we used EGFs merged with SGFs together with finite rupture models instead of standard "attenuation relations" and included all considerable-magnitude earthquakes. Wave propagation was simulated with an approach based on a Green's functions (GF) algorithm that satisfies source- and site-specific estimation of full-waveform time histories. All of the mathematical calculations were done by the computer programs explained in Hutchings et al. (2007).

In the past 50 years, especially after the work of Cornell (1968) and Algermissen et al. (1982), the earthquake hazard concept has included consideration of uncertainties, such as in the location of earthquakes, the size of earthquakes, and the recurrence relationship of earthquakes, based on probabilistic calculation. PSHA is the most convenient method for identifying or quantifying these uncertainties to provide a comprehensive solution of the earthquake ground motion parameters at a particular site. Mostly, these parameters classify as peak acceleration or spectral response. To understand clearly the PSHA concept, which can be described as a four-step procedure, requires not only a familiarity with terminology but also a basic understanding of probability theory. The first of the four steps is identifying earthquake sources to determine distances between site and hypocenter and to characterize these to clarify any expected earthquake. The second step is to characterize the seismicity and distribution of earthquakes not only spatially but also temporally to determine the recurrence relationship, which is defined as the average rate of earthquakes of various sizes for each source zone. Next, using empirical attenuation relationships, one may predict the distribution of ground motion intensity as a function of magnitude and distance. Finally, using the outputs of the first three steps as an input and the calculation procedure known as the probability theorem, all of the parameters are combined to produce a hazard curve. The PSHA methodology used in this study uses the same procedure as standard PSHA and risk analysis except for the third step. Instead of using empirically derived attenuation relationships to predict ground motion parameters such as peak ground acceleration (PGA) or spectral acceleration, we directly calculated synthetic seismograms. This procedure is discussed further in a publication of the Senior Seismic Hazard Analysis Committee (SSHAC 1997).

The most outstanding aspect of this methodology is that earthquake hazard or risk can be estimated from fault rupture and can be implemented directly to building response. It does not require sufficient historical earthquake waveforms, or an empirical formulation that represents the physical properties of the medium, or geological information. Another advantage of this methodology is the reduction in uncertainties. Generally, the PSHA methodology contains two different uncertainties. One is epistemic uncertainty, which can be defined as the unpredictability of different physical properties or factors associated with the earthquake rupture process. Our estimation is basically based on epistemic uncertainty, and this type of uncertainty can be reduced by different investigations that are focused on the earthquake fault mechanism and rupture process. Aleatory uncertainties can be explained as the connatural, or inherent, randomness of a procedure. Because of its inherent nature, it is not possible to reduce these types of uncertainties. The regression approach that is generally used to estimate different ground motion parameters in classic PSHA calculation is based primarily on aleatory uncertainty. In this study, we used a physically based PSHA approach that not only estimates source and site-specific calculations of full-waveform ground motion time histories that are significant for nonlinear dynamic analysis of structures but also decreases uncertainties in the evaluation of standard engineering parameters.

Simulation methodology

In order to obtain the necessary simulated ground motions with the intention of dynamic analysis of engineering structures and earthquake response and thus risk, we achieved earthquake simulations. The physically based ground motion simulation approach proposed by Hutchings and Wu (1990) and Hutchings (1991), and further expanded and developed by Hutchings et al. (2007) and Scognamiglio and Hutchings (2009), was applied. The methodology was termed "physically based" because it considers the physics of fault rupture and the wave propagation process to simulate ground motion time histories. Fault rupture processes are represented by the elastodynamic equation of seismology and fracture energy and with a physical understanding of how a fault ruptures, as explained by Hutchings et al. (2007). These models are mostly explained as quasi-dynamics models (Boatwright 1981), which depend on field observations, laboratory experiments, and numerical modeling. The methodology has been validated several times (Hutchings and Wu 1990; Hutchings 1991; Heuze et al. 1994; Hutchings 1994; Foxall et al. 1996; Hutchings and Jarpe 1996; Hutchings et al. 1997, 1998, 2007; Jarpe and

Kasameyer 1996; Rosset et al. 1998; Wossner et al. 2002; Scognamiglio and Hutchings 2009; Nicknam and Eslamian 2011; Golara and Jazany 2013; Papoulia et al. 2015).

A discretized representation relation along with Green's functions is used to obtain synthetic seismograms. To model finite fault rupture, which utilizes Green's functions, the exact solution of the representation relation can be used. As explained by Hutchings and Wu (1990), the methodology considers that Green's functions are defined as effectively impulsive point sources and that any variation of their stress drop is reflected only in the differences of their seismic moment. Hutchings et al. (2007) specified that "effectively impulsive point source refers to the observation that factors such as rise time, rupture duration, or source dimension are small enough that their effect cannot be observed in the frequency band of interest."

In the source area, for each small area or grid, Green's functions are convolved with synthetic slip functions and summed to obtain synthetic ground motion waveforms originated from the extended source earthquake. A schematic representation of earthquake simulation developed using GFs is provided in Fig. 2.

The discretized representation relation can be written as:

$$u_n(X,t) = \sum_{i=1}^{N} \frac{\mu_i A_i S(t')_i}{M_{0\,i}^{e}} \times e_n\left(X,\ t' - t_r\right)_i. \qquad (1)$$

This is the equation by which synthetic seismograms are calculated. It is the exact solution for the representation relation under certain conditions, and it was our intent to stay as close as possible to the mathematically exact solution, with approximations adding to the uncertainty of the solution. The equation was described in detail by Hutchings et al. (2007).

Calculation of earthquake source parameters used as empirical Green's functions

Calculating the moment and corner frequency of the source events used in strong ground motion synthesis with empirical Green's functions is important for increasing the predictive reliability of strong ground motion. The approaches of Irikura (1986), Hutchings and Wu (1990), and most other others add up or scale empirical Green's functions based on the moment estimate of the small events. However, the source corner frequency is used differently in different methods. In our method, the corner frequency is necessary in order to deconvolve out the Brune source function to create effective impulsive point source events. Then, when EGFs are used in Eq. 1, the shape of the high-frequency falloff of the synthesized seismograms is determined by the rupture parameters (Hutchings 1991). Additionally, no assumption is made about the stress drop of the small EGF. Most other methods assume that the stress drop of the synthesized earthquake is the same as that of the EGF.

To estimate the source parameters (moment M_o, source corner frequency f_c, and attenuation parameter t^*) of the earthquakes used, an EGF simultaneous inversion (Hutchings 2001) was conducted. Simultaneous inversion basically depends on the assumption that for a specific earthquake the corrected long-period spectral levels and the source corner frequencies must be equal at all of the different recording locations. The reason for the differences in the spectra can be explained by propagation path, individual site attenuation, and site response.

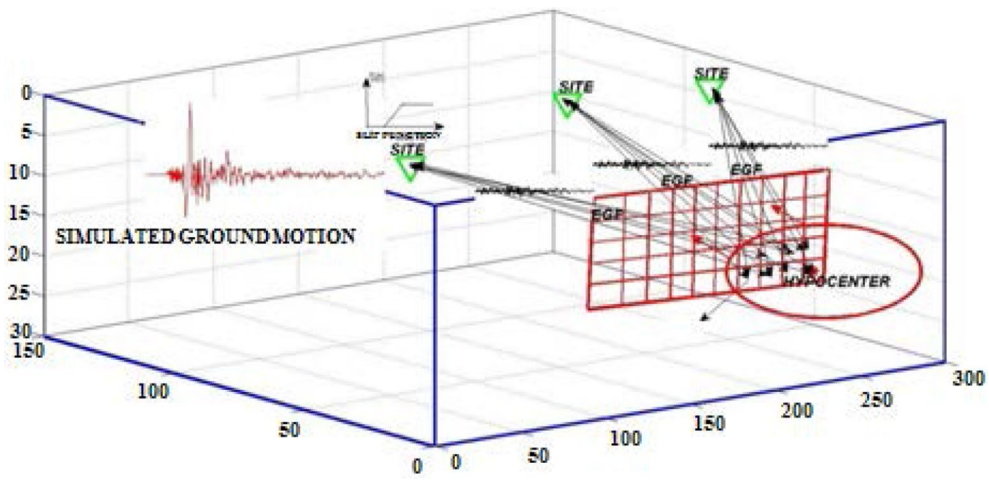

Fig. 2 Schematic illustration of Green's function simulations

To calculate the source parameters of an earthquake (M_o, f_c, t_g^*), the displacement spectra obtained from the S-wave waveform of the recorded seismograms were fitted to the Brune (1971) displacement spectral shape with a site-specific attenuation operator by using a nonlinear least squares method. The spectra calculated from the recorded seismograms were corrected to characterize the moment at the long-period asymptote and for whole path attenuation. The correction to spectra prior to the joint inversion was based on the equation for moment by Aki and Richards (1980, p. 116). The free surface correction factor was determined from the one-dimensional velocity model using the reflection coefficients, as outlined in Aki and Richards (1980, p. 190). The spectra of the recorded seismograms were corrected by

$$\Omega^{'}(f)_i = \frac{4\pi\pi^{\alpha}\rho_{x^{1/2}}\rho_{\zeta^{1/2}}\beta_{x^{1/2}}\beta_{\zeta^{5/2}}}{S^S F^S} U(f)\exp(-\pi f t_r). \tag{2}$$

The recorded spectra were then fit to the Brune (1971) displacement spectral shape with site-specific attenuation (t_g^*) and moment as the long-period spectral asymptote. The spectra were fit to the modified Brune spectra:

$$\Omega(f) = \frac{\mathrm{M}_o \exp(-\pi f t_g)}{\left[1+\left(\frac{f}{f_c}\right)^2\right]}, \tag{3}$$

where M_o is the moment, f is the frequency, f_c is the source corner frequency, and t_g^* is the site-specific attenuation. The best-fitting model of the source parameters (M_o, f_c, t_g^*) was obtained by iteration from a starting model using the simplex algorithm (Nelder and Mead 1965; Caceci and Cacheris 1984, Numerical Recipes 1998, Chap. 10.4). Further information and more detailed explanation about the methodology for calculating source parameters of an earthquake can be found in Hutchings (2001) and Gök et al. (2009).

Calculation of Synthetic Green's Function

Because small earthquake records used as EGF are band-limited by instrument response and cultural noise, they do not include energy below 0.5–1 Hz. For this reason, SGFs were calculated to provide the low-frequency energy to the simulated ground motion. To produce SGFs, an explicit 2D/3D elastic finite difference wave propagation code was used. This code, named E3D, developed by Larsen at the Lawrence Livermore National Laboratory, computes realistic simulation of elastic waves in a 3D geologic model.

The main framework of the code is based on the elasto-dynamic formulation of the full-wave equation on a staggered grid. An explicit finite difference scheme is used to analyze the velocities v_i and the stress tensor components τ_{ij}. Using summation notation over repeated indices $_i$, the basic equations are given by:

$$\begin{aligned} v_i &= 1/\rho\left(\tau_{ij,j} + f_i\right) \\ \tau_{jj} &= \lambda \cdot v_{ii} + 2\mu \cdot v_{jj} + m_{jj} \\ \tau_{ij} &= \mu \cdot \left(v_{i,j} + v_{j,i}\right) + m_{ij}, \end{aligned} \tag{4}$$

where ρ is the density, μ is the rigidity, and λ is the Lame parameter. Body force functions f_i and/or seismic moment rates m_{ij} are used as source terms to drive the velocities and stresses. More detailed explanations related to the theoretical background of E3D can be found in McCallen and Larsen (2003).

Empirical Green's functions data

The dataset was composed of nine small earthquakes ($2.5 \leq M_w \geq 3.3$) that occurred on the PIF, which is one of the main extensions of the northern branch of the NAFZ in the Marmara Sea (Fig. 3). This dataset was recorded by a broadband seismometer network operated by the Bogazici University-Kandilli Observatory and Earthquake Research Institute (BU-KOERI). Table 1 lists the origin times, hypocenters of the events reported by the BU-KOERI, and the source parameters calculated in this study. The names and locations of the stations used to calculate the source parameters of the earthquakes are shown in Fig. 3 and listed in Table 2.

Physically based probabilistic hazard analyses

Source Parameters of Empirical Green's Functions

The source parameters (M_o, f_c, and t^*) of an earthquake, used as EGFs, were calculated directly from the horizontal components of S waves. Figure 4 illustrates how the spectra were fitted simultaneously for source and individual station. The solid red line indicates the modified Brune model over the frequency band that we used. The actual moment is the projection of this fit to asymptotic low frequency. In Fig. 4, we used the 2009.02.21 22:29 earthquake to fit the Brune spectrum and recorded the spectrum in the frequency range between 1 and –15 Hz.

Before performing the inversion, the signal-to-noise ratio (SNR) of the recorded waveform was determined, and only the frequency ranges above a selected SNR were used to fit the Brune model to the recorded spectra. To calculate the source parameters of the selected earthquakes, the SNR value of 10 was used. Table 1 lists the source parameters of the earthquakes used as an EGF.

During the analysis, the horizontal components of the recorded seismograms were converted to the radial and transverse components, and then the first 6 s of S waves was used to compute the source displacement spectra. For each earthquake, the source parameters were computed using simultaneous inverse solution techniques, as

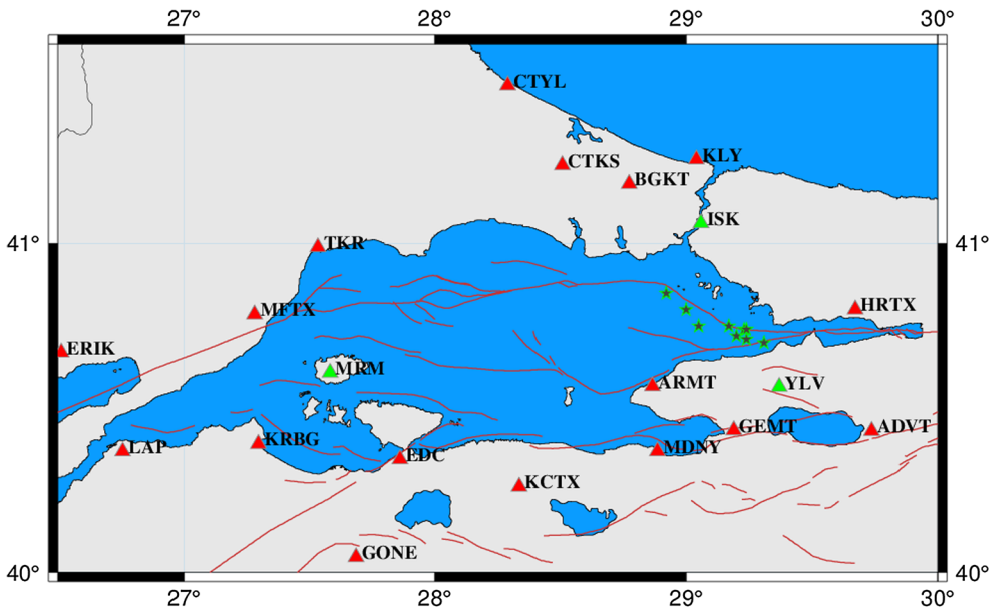

Fig. 3 Earthquakes used to obtain empirical Green's functions (*green stars*) and recording broadband stations (*red triangles*). *Green triangles* show three stations that we calculated the uniform hazard *curve*

Table 1 Source parameters of earthquakes used as an empirical Green's function

EQ	Date	Lat (N)	Long (E)	Depth (km)	Moment (dyn-cm) x 10**20	f_c	M_w
E01	2004.05.16 21:07	40.70	29.31	9	9.08 ± 1.27	13.8 ± 3.7	3.3
E02	2005.02.23 10:37	40.85	28.92	23	3.38 ± 5.56	15.6 ± 4.3	3.0
E03	2005.09.08 00:22	40.72	29.20	12	1.03 ± 0.43	5.6 ± 0.0	2.6
E04	2005.09.08 03:39	40.71	29.24	5	2.83 ± 0.75	4.9 ± 0.6	2.9
E05	2005.09.07 13:22	40.74	29.23	9	7.00 ± 6.13	4.1 ± 0.2	3.2
E06	2005.09.07 13:50	40.74	29.24	19	8.14 ± 6.82	4.4 ± 0.1	3.2
E07	2006.09.12 18:18	40.80	29.00	11	2.70 ± 0.87	16.6 ± 2.5	2.9
E08	2009.02.21 22:29	40.75	29.05	14	2.79 ± 3.61	3.9 ± 0.2	2.9
E09	2010.09.19 15:05	40.75	29.17	9	0.54 ± 0.69	11.7 ± 4.4	2.5

explained in "Methodology" section. In order to eliminate the effects of damping at certain frequencies between the stations along the path, they were recorded with respect to the earthquake sources (the available studies in the literature regarding the Marmara region were reviewed). The frequency-dependent quality factor of the shear waves relationship, $Q(f) = 180\, f^{0.45}$, proposed by Akinci et al. (2006) was utilized. The wave propagation geometrical scattering effects (R^{α}) on the displacement spectra were removed using the factor $\alpha = 0.5$ for distances greater than 100 km and $\alpha = 1.0$ for distances less than 100 km. The 1D shear velocity model proposed by Karabulut et al. (2003) was used in the analysis. The free surface correction coefficient (S) was computed form the shear velocity model. To compute density values from the P wave velocity (V_p), the relationship of Lama and Vutukuri (1978) was used. The focal mechanism radiation correction factor (F) of 0.47 and 0.52 (Prejean and Ellsworth 2001) was used for SV and SH arrivals, respectively. The local soil effects on the displacement spectra could not be removed because the soil response functions were not known. Therefore, local site effects are considered to be the reason for the scattering of the results.

Synthetic Green's Functions for Low-frequency Simulations

In order to perform broadband simulation for different earthquake scenarios of the PIF, the low-frequency synthetic Green's functions needed to be generated.

Table 2 Station information

No.	ST ID	Location	Lat (*N*)	Long (*E*)	Elev (*M*)	Instrument
1	ADVT	Abdülvahap, Iznik	40.433	29.738	193	3ESP-DM24
2	ARMT	Armutlu, Yalova	40.568	28.866	320	3ESP-DM24
3	BALB	Balikesir	39.651	27.864	120	3T-DM24
4	BGKT	Bogazköy, Istanbul	41.181	28.773	80	3ESP-DM24
5	CTKS	Kestanelik, Çatalca	41.2363	28.5067	47	3ESP-DM24
6	CTYL	Yaliköy, Çatalca	41.476	28.2897	77	3T-DM24
7	EDC	Edincik, Balikesir	40.3465	27.8618	257	3T-DM24
8	EDRB	Edirne	41.847	26.7437	209	3T-DM24
9	ENEZ	Enez, Edirne	40.7362	26.153	100	3T-DM24
10	ERIK	Erikli, Çanakkale	40.6708	26.5132	38	3ESP-DM24
11	EZN	Ezine, Çanakkale	39.8255	26.3247	48	3ESP-DM24
12	GADA	Gökçeada, Çanakkale	40.1908	25.8987	59	3T-DM24
13	GELI	Gelibolu, Çanakkale	40.398	26.4742	126	3ESP-DM24
14	GEMT	Gemlik, Bursa	40.435	29.189	220	3T-DM24
15	GONE	Gonen, Balikesir	40.0467	27.686	140	3ESP-DM24
16	GULT	Gölveren, Sakarya	40.4322	30.5153	942	3ESP-DM24
17	HRTX	Hereke, Kocaeli	40.801	29.673	573	3ESP-DM24
18	**ISK**	**Kandilli, Istanbul**	**41.0615**	**29.0592**	**132**	**3T-DM24**
19	KCTX	Karacabey, Bursa	40.2627	28.3353	445	3ESP-DM24
20	KLY	Kilyos, Istanbul	41.0638	29.06	30	3T-DM24
21	KRBG	Karabiga, Çanakkale	40.3932	27.2977	79	3ESP-DM24
22	LAP	Lapseki, Çanakkale	40.3703	26.7593	230	3ESP-DM24
23	MDNY	Mudanya, Bursa	40.371	28.8847	116	3ESP-DM24
24	MDUB	Mudurnu, Bolu	40.4712	31.1977	1109	3T-DM24
25	MFTX	Murefte	40.7867	27.2812	924	40T-DM24
26	**MRM**	**Marmara Adasi**	**40.609**	**27.5832**	**702**	**3T-DM24**
27	SPNC	Sapanca, Adapazari	40.686	30.3083	190	3ESP-DM24
28	TKR	Tekirdağ	40.9893	27.535	140	3ESP-DM24
29	**YLV**	**Yalova**	**40.5658**	**29.3708**	**879**	**3T-DM24**

Bold values indicate stations that physically based ground motion simulations were realized to obtain uniform hazard spectra

For this purpose, a three-dimensional volume with a length of 360 km in the east–west direction, a width of 220 km in the north–south direction, a height of 30 km in the vertical direction, and a starting point of 40.0 N, 26.40 E was introduced (Fig. 5). The dimensions were selected to include all stations for the simulations. The PIF was placed at the coordinates of 40.8907 N, 28.7831 E and 40.7 N, 29.3900 E, with a fault width of 15 km and a fault depth of 10 km from the surface. The shear velocity model proposed by Karabulut et al. (2003) was used for the simulation. The proposed station locations for the simulations were placed at the surface of the volume, taking into account their spatial coordinates.

The earthquake sources were placed laterally on the fault every 7 km and at three depths (12.5 km, 17.5 km, and 22.5 km); therefore, 24 earthquake sources were used to produce the synthetic Green's functions. The seismic moment of the earthquake source was considered to be M_o = 1e+21 dyn.cm (considering an M_w = 3.0 earthquake), and the corner frequency was 3.3 Hz. The fault mechanism of the earthquake sources was chosen to be compatible with the PIF mechanism with strike of 118°, dip of 90°, and rake of −180°. The volume was discretized with 0.5-km grids, and a time step of 0.02 was chosen for the output synthetic seismograms. Figure 6 shows the generated synthetic seismograms of station ISK.

Earthquake hazard and synthetic rupture models

The classical PSHA methodology was introduced by C. Allin Cornell in his milestone paper of 1968 and developed further by contributions from McGuire in 1976. The core of PSHA lies in the integration of individual influences of potential earthquake sources (considering both size and distance) into the probability distribution of the maximum annual ground motion parameter, from which the return period follows (Cornell 1968). The recurrence

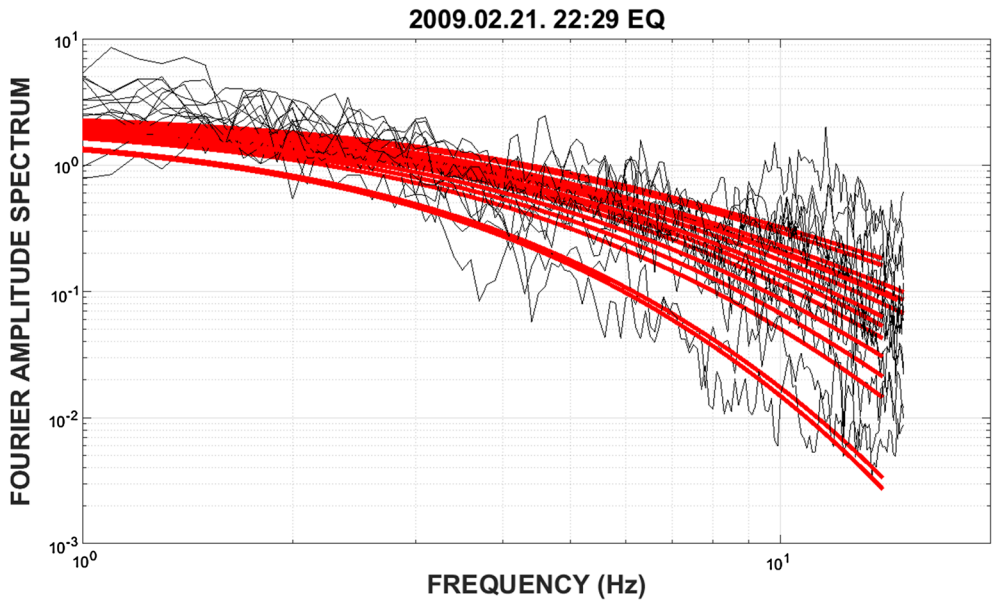

Fig. 4 Theoretical Brune spectra fitted to the corrected S waves displacement spectra of the recorded earthquake. The radial and transverse components of S waves of stations ADVT, ARMT, BALB, BGKT, CTKS, CTYL, EDC, GONE, HRTX, ISK, SPNC, KCTX, MDNY, and MDUB were used

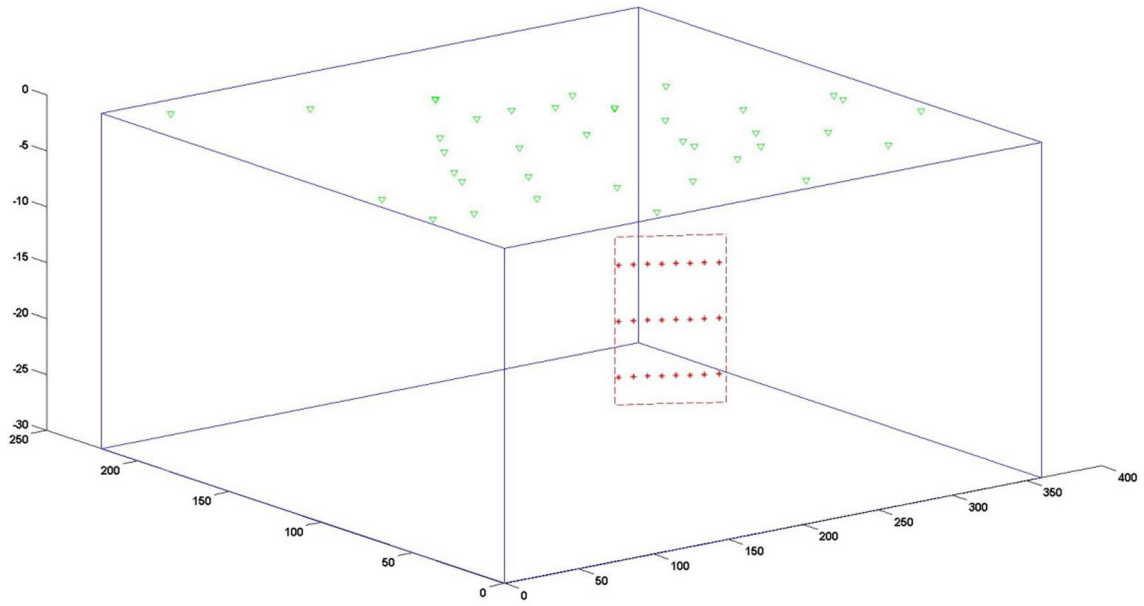

Fig. 5 Finite difference model for synthetic seismograms of the Prince Islands Fault. *Red stars* are earthquake source points, and *green triangles* are station locations

rate of earthquakes was assumed to follow the cumulative Gutenberg–Richter relation:

$$\log N(M) = a - b\,M. \tag{5}$$

Ground motion descriptors such as peak ground acceleration (PGA) were calculated from ground motion prediction equations (or attenuation relationships), and the mean rate of exceedance of a specified ground motion amplitude, which is the hazard, was determined.

The definition of the seismic source model was developed based on the spatial distribution of earthquake events of the collected and processed catalog and the tectonic

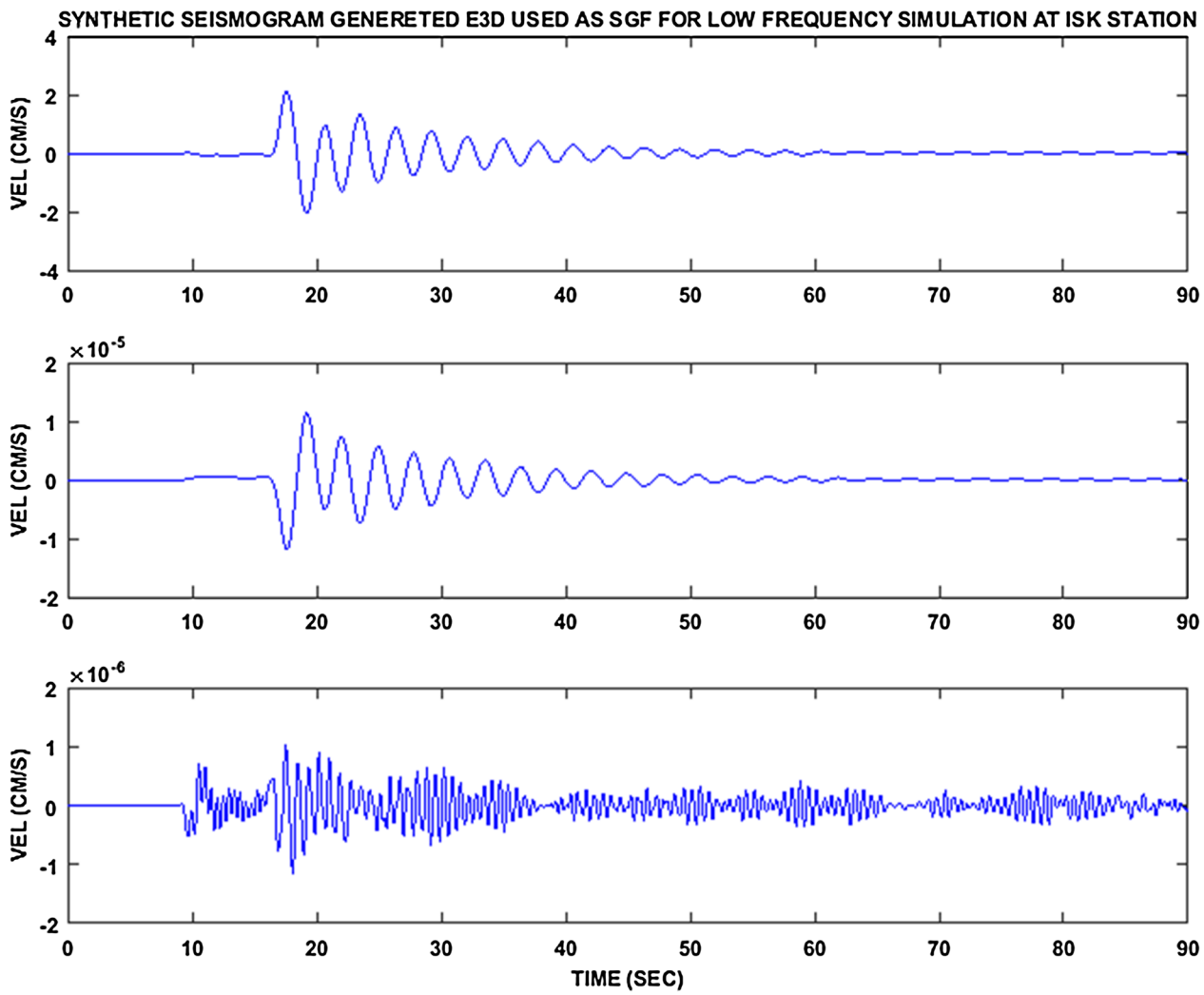

Fig. 6 Synthetic seismogram generated E3D used as SGF for low-frequency simulations at Station ISK

and deformational pattern. In this study, to apply classical PSHA, an attempt was made to build a coherent earthquake catalog, considering the criteria of Oncel and Alptekin (1999), using data from the Kandilli Observatory and Earthquake Research Institute (KOERI). Our catalog for the study was composed mainly of reported instrumental events covering the period from May 12, 1901, to July 31, 2015. A basic assumption of conventional seismic hazard methodology is that earthquake sources are time independent (i.e., random distribution in time). Thus, catalogs must be free of dependent events such as foreshocks and aftershocks, which are by definition both time and space dependent relative to the mainshock. There are many different algorithms that attempt to identify triggered earthquakes and remove them, a process that is often called declustering. We applied the procedure of Gardner and Knopoff (1974) to eliminate foreshocks and aftershocks from the catalog.

For a forecasting experiment like the one of this study, the completeness of the catalog is important because many models assume a complete catalog to estimate their parameters. The minimum magnitude of complete recording (M_c) is an important parameter for most studies related to seismicity. In order to achieve the objectives of this study, the catalog was investigated for duplication, completeness, and time independency of its event distribution. The magnitude of completeness (M_c) based on the maximum curvature method (Wiemer and Wyss 2000) and the a value and the b value were determined from a frequency magnitude distribution. Figure 7 shows the declustered earthquake catalog and the seismic source models that we used for the region. The blue area was selected for the regional seismic source area, based on previous studies (Demircioglu 2010), and was used to calculate b value, which is a regional parameter. The red line

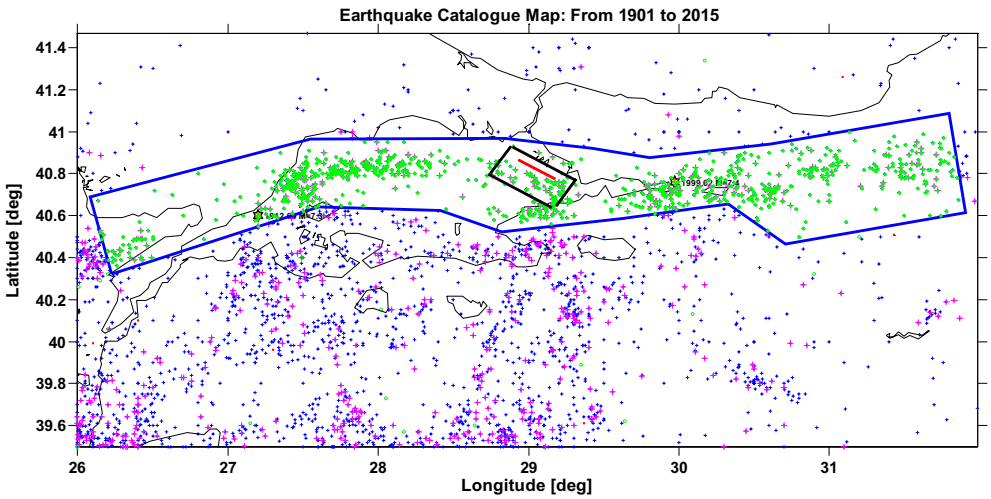

Fig. 7 Seismic source zones and declustering process of catalog (*red circles* indicate removed aftershocks and foreshocks)

indicates the Prince Island Fault, and the black rectangular area around it shows the area that we used to calculate a value for the Prince Island Fault. The b value ($b = 0.9$), which is compatible with previous studies, and the inclination of the linear regression were calculated by using the regional seismic source area. The a value ($a = 3.3$) is the value at which the line intercepts the y axis and is also called the productivity. (M_c) is the lowest value at which the distribution still has linear form (Fig. 8).

In the framework of the newly proposed methodology of this study, which depends on physically based ground motion simulation, we developed different rupture scenarios for all considerable-magnitude earthquakes throughout the PIF. The rupture scenarios were selected randomly with varied independent rupture parameters. The variation of the rupture parameters was determined, considering the physical limits, by using different independent researches in the literature (Wells and Coppersmith 1994; Somerville et al. 1999).

Considering the seismic activity along the PIF, we generated a synthetic catalog long enough for all considerable earthquakes in order to calculate every possible

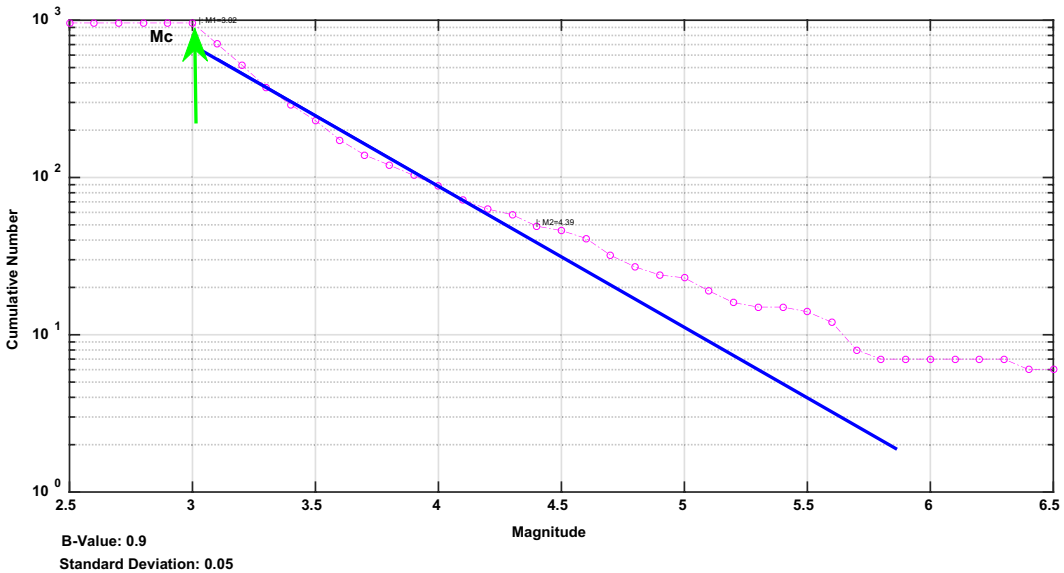

Fig. 8 Frequency magnitude distribution for regional seismic zone. The *pink circles* show the cumulative number of earthquakes. The *green arrow* shows the estimated magnitude of completeness, and the *blue line* shows the estimated parameters of the Gutenberg–Richter law

ground motion waveform. For this purpose, we considered the b value and the range of specified magnitudes. In this case study, the PIF synthetic catalog range and the duration of the catalog were selected from $M_w = 4.0$ to 7.0 and 30,000 years, respectively.

To generate rupture scenarios for the range of simulated earthquakes, parameters were selected using the Monte Carlo selection method. The different rupture parameters such as rupture geometry, rupture velocity, rupture roughness, hypocenter location, moment, number and size of asperities, and healing velocity used to create the rupture scenarios were generated using the computer program HAZARD developed by Hutchings (2006). Values for parameters were selected randomly from the uniform distribution. Strike, dip, and slip vectors were selected from triangular distributions about preferred values. For each set of scenarios, moment and fault geometry were fixed, and some other parameters, e.g., rise time, stress drop, and energy computed, depended on rupture characteristics and so were termed dependent variables. The high-frequency energy variability of the generated synthetic waveforms depends on short wavelength (asperities) or short time duration (rise times and roughness). Similarly, the variability in low-frequency energy depends on longer-scale changes due to focal mechanism radiation variation or long scale-length finite fault effects such as directivity and moment (Hutchings et al. 2007).

We now characterize the parameters, based on the seismic activity and the characteristic behavior of the PIF, that are subsequently used as input during the simulation process (Wells and Coppersmith 1994; Somerville et al. 1999; Pinar et al. 2003; Örgulu 2011). We computed synthetic seismograms for about 700 rupture scenarios for a range of earthquakes. The obtained synthetic seismograms will be the basis of our hazard calculation. We did not need to calculate each synthetic waveform from the small-magnitude events because the rupture characteristics of small earthquakes are much simpler and repeat a similar scenario much more frequently than larger earthquakes' scenario.

Moment The values of the moment and the corresponding moment magnitudes were calculated according to the relation of Hanks and Kanamori (1979). For each scenario, seismic moments were computed using moment magnitude increments of 0.5 units from $M_w = 4.0$ to 7.0 (0.107×10^{23} to 0.372×10^{27} dyn-cm). If the rupture model included asperities, the asperity moment was chosen randomly. Rigidity values depended on the shear wave velocity for all depths. Because rigidity decreases near the surface, the moment contribution also diminishes close to the surface.

Hypocenter Locations for each scenario were changed randomly along the fault hazard area. We used some constraints to select hypocenter locations, namely at least 10 % of the fault length from the fault edges, in the lower half of the fault, and at depth greater than 6 km, based on seismic activity studies conducted for the PIF considering a long-term observation period (Bohnhoof et al. 2013).

Strike, dip, and slip Considering the geometrical spreading of the PIF, which is a SW–NE-trending strike-slip fault in the vicinity of the Marmara Sea, the strike for the possible rupture scenarios was taken as 290° ± 10°. According to the observed long-term microseismic activity, the dip and slip vector were chosen as 45° ± 15° and 124° ± 20°, respectively.

Fault rupture geometry The form of the fault was restricted to be rectangular. The length and width of the geometry were constrained to 45 ± 3 km and 15 ± 3 km, respectively. For small earthquakes, this range varied by between 0.5 and 1.0 km.

Slip distribution The slip distribution was changed in two different ways. First, the Kostrov slip model with healing was used because this model allows variable rise time and slip amplitude, but constant stress drop. Second, smaller areas with high slip amplitudes and high stress drops were called asperities.

Asperities Asperities were selected as circular areas characterized by high slip amplitudes and high stress drops along the rupture surface. The number of asperities and their diameter, 0.2 to 0.8 times smaller than the main axis of the rupture, were selected randomly for each scenario.

Rupture roughness Rupture roughness was simulated as elements first resisting rupture and then breaking. A percentage of elements (0, 10, 33, or 50 %) had shortened rise times between 0.1 and 0.9 times the original value or those of neighboring elements, but with rupture completed at the same time. This distributed randomly on the fault because of the radial arrangement of elements. Areas of roughness, or "rough" elements, were also another portion of the surface rupture that had high stress drop [i.e., the Schulz (2002) model of contact asperities].

Rise time The rise time is the time from the initiation of fault rupture for the first healing phase to arrive. It can be defined as the shortest time required for the rupture front to reach an edge and a healing pulse to return to the element. Rise time varies at each point on the fault surface.

Rupture velocity This variable was chosen randomly depending on the shear wave velocity. Rupture velocity varied from 0.75 to 1.0 times the shear wave velocity.

Healing velocity The velocity of the stress pulse that terminates slip is called the healing velocity. The healing phase begins after rupture reaches any fault edge. It was selected randomly within the range of 0.8 and 1.2 times the rupture velocity.

Stress drop This is a significant parameter that affects the amplitudes of the synthesized waveforms, and it is a dependent parameter based on the Kostrov slip function. The stress drop along the rupture surface depends on three different conditions, as mentioned above. Within asperity areas and within rough elements, the stress drop has higher values; and near the surface, it is constrained to diminish.

Earthquake simulations

To generate the high-frequency part of the broadband earthquake simulation, the real recorded earthquakes were used as EGF. Here, an important point is the precision of the EGFs at higher frequencies because their displacement source spectra were smooth up to the highest frequency of interest. They also included real effects of velocity structure, attenuation, and geometrical spreading so that they characterized the path effect correctly at high frequencies. Furthermore, the recorded Green's functions also included information about the linear response of the upper soil. These are the main advantages of the simulation algorithm used.

However, it usually is not possible to utilize EGFs to obtain full broadband simulations because small earthquakes records (EGFs) are band-limited and do not have information below 0.5 Hz. In order to produce broadband simulations for the different earthquake scenarios of the PIF, for the frequency range 0.5–20 Hz, the simulations were calculated using by EGFs, and for the frequencies below 0.5 Hz, the simulations were obtained using by SGFs, which were synthetic seismograms calculated by an explicit 2D/3D elastic finite difference wave propagation code (Larsen 1995) named ED3. During the simulations, EGF and SGF were scaled linearly according to differences in seismic moments.

The rupture surface area was discretized into 0.05 km^2 elemental areas that were small enough to obtain continuous rupture for frequencies up to 20 Hz. The linearly increasing velocity model developed by Karabulut et al. (2003) was preferred to synthesize the earthquakes. The velocity variation of P wave from the surface of the earth to depth followed the equation $V_p = 0.0788z + 5.4$, with a velocity value of 8 km/s at the depth of 33 km. In order to avoid unnecessary and unreasonably large slip at the earth surface, the depth of the upper edge of the rupture area was set to 2.0 km.

The distribution of small earthquake sources at the fault surface to represent the propagated energy from all of the regions across the fault surface was practically not possible. During the simulations, interpolations of the recorded AGFs and calculated SGFs for all of the regions across the fault surface were performed. Another important point for the use of representation relations is that the selected earthquakes used as EGF or SGF must provide effectively impulsive point source conditions or, in other words, their moment must be below a threshold (about 1.5×10^{14} Nm) (Hutchings and Wu 1990; Hutchings 2001). If the moment value of the earthquake used as the EGF is larger than the threshold, it is useful to deconvolve out the source effect from the spectrum to provide an effective impulsive point source (Hutchings et al. 2007). This procedure was applied to some of the EGFs used in this study.

Merging Procedure of Empirical and Synthetic Green's Functions

To obtain a broadband simulation, a merging procedure was applied. In the literature, several methods for this purpose have been developed in earthquake engineering applications (Irikura and Kamae 1994; Beresnev and Atkinson 1997; Kamae et al. 1998; Hartzell et al. 1999; Pitarka et al. 2000; Graves and Pitarka 2004; Pulido and Kubo 2004; Liu et al. 2006; Mena et al. 2006; Pulido and Matsuoka 2006; Rodgers et al. 2008; see Mai et al. 2010). In broadband earthquake simulation spectra, for frequencies below 0.5 Hz, the simulations are obtained by low-pass filtering the SGF seismograms, whereas for the frequency higher than 0.5 Hz, the simulations are obtained by high-pass filtering of the EGF functions.

Integrating the low- and high-frequency synthesized components, we obtained broadband earthquake simulations using an in-house merging algorithm developed under the MATLAB environment. The frequency range of the synthesized broadband waveforms calculated from each scenario was 0.1 Hz to 20.0 Hz for all necessary stations. The sampling rate of the earthquake records used as EGFs in the high-frequency band was 0.02 s, which thus provided high-frequency components up to 25 Hz Nyquist frequency in the spectra. However, because of the noise level characteristics of the smaller-sized earthquakes, the preferred frequency band was selected as 0.5–20 Hz, and in the merging algorithm, we used the 0.5 Hz frequency as the pivot frequency. The GF synthetics at low frequencies (0.1–0.5 Hz) calculated using the finite difference algorithms yielded reliable results by taking into account the grid size (0.5 km) and the structural features of the seismic velocity model. To combine the low- and high-frequency synthesized components, at a merging corner frequency, we applied a low-cut filter for low-frequency waveforms and a high-cut filter for high-frequency waveforms. During the merging process, to select proper filtering coefficients, the code also considered that the sum of the merged filtering function in the frequency domain would be approximately unity. Thus, the merged synthesized broadband waveforms did not include spurious amplitudes around the merging frequency.

To control the merging procedure, we generated and applied a known harmonic motion that was composed of different amplitudes sinusoid for different frequencies.

Then, we obtained exactly the same amplitudes at the same frequency. The filter functions used here are defined in Fig. 9, and the merging procedure is explained in Fig. 10. In the example, the given station is YLV (horizontal component). The blue-colored seismograms in the first column of the figure are the low-frequency SGF simulations, and the red-colored seismograms are the filtered simulations derived by using the filter function shown in Fig. 9. The second column shows the high-frequency original and filtered simulations, and the third column indicates the original and the filtered seismograms obtained from the low- and high-frequency components of the simulations.

Discussion and conclusions

The main motivation of this study was that the inevitability of the occurrence of a large earthquake along the PIF in the Marmara Sea increases the earthquake disaster risk around the Marmara region, especially in Istanbul. The specific study reported herein was essentially intended to estimate a PSHA using broadband strong ground motion simulations within the Marmara region, Turkey, from potential earthquakes along the PIF segments in the Marmara Sea.

Unlike current PSHA approaches that use regression of empirically derived parameters that are described by probability distributions and thus include aleatory uncertainty, the methodology used in this paper depends basically on physical parameters that characterize the earthquake rupture process and thus includes epistemic uncertainty explained by the variability in the physical parameters of the rupture process. It is possible to increase our knowledge of the earthquake rupture process by research, so it is possible to reduce the epistemic uncertainty within PSHA in order to reduce the uncertainty level of the calculated hazard. Aleatory uncertainty is caused by inherent randomness of process and results in parameters without boundaries, and thus it is not possible to reduce aleatory uncertainty.

A physics-based rupture process and a quasi-dynamic rupture model were used to obtain ground motion waveforms that might be generated by earthquakes with a certain range of magnitudes ($4 \leq M_w \geq 7$) rupturing the PIF segment of the North Anatolian Fault crossing the Marmara Sea. We simulated the broadband (0.1–20.0 Hz) synthetic seismograms for three locations (Table 3). Small earthquake records were used as EGFs to obtain ground motion simulations for the frequency range of 0.5–20.0 Hz. For the frequency range of 0.1 to 0.5 Hz, we need to compute SGFs to obtain ground motion simulations. We utilized the finite difference code E3D to synthesize SGFs. To combine the low- and the high-frequency synthesized waveforms obtained by using each earthquake scenario at each station, we used an in-house merging algorithm. By varying the rupture parameters within prescribed limits, we created a library of synthetic seismograms for each site and applied them to perform physics-based PSHA.

In the framework of this research, we developed a range of rupture scenarios for all considerable-magnitude earthquakes throughout the PIF by randomly varying the independent rupture parameters within the ranges of physical limits obtained from independent research (Wells and

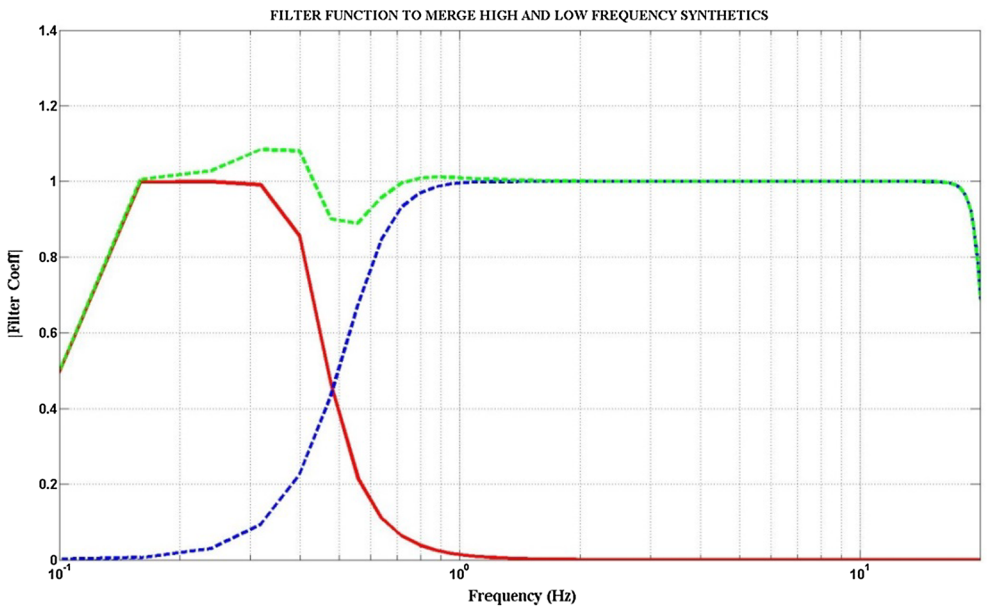

Fig. 9 Filter functions used to obtain the broadband earthquake simulations

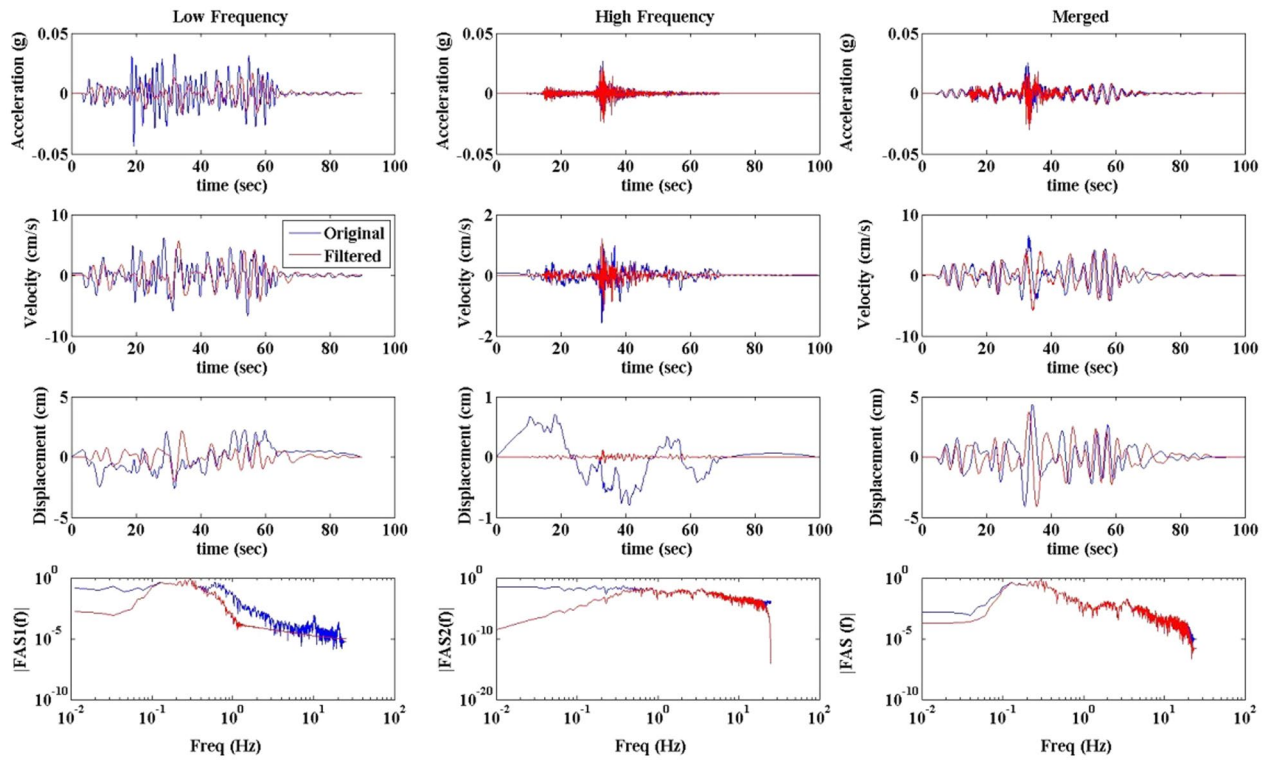

Fig. 10 Integration of the simulation results obtained for low- and high-frequency bands at Station YLV (*blue color* is the original seismogram, and *red color* is the filtered seismogram)

Table 3 Stations for which we simulated broadband synthetic seismograms and calculated hazard curves

ST ID	Location	Latitude (*N*) (Deg)	Longitude (*E*) (Deg)	Elevation (m)	Type
ISK	Edincik	41.0615	29.0592	132	3T-DM24
MRM	Marmara Adasi	40.6058	27.5837	213	3T-DM24
YLV	Yalova	40.5658	29.3708	879	3T-DM24

Coppersmith 1994; Somerville et al. 1999). Here, we created a synthetic catalog long enough to represent all considerable earthquake scenarios to characterize the activity of the PIF for the purpose of calculating all possible ground motion.

Another advantage of this method of using a synthetic catalog long enough to represent all considerable earthquakes is that we generated a library of seismograms. These full-waveform estimations can be used not only to develop hazard curves of traditional engineering parameters in the form of annual probability exceedance but also to develop risk estimates that can be applied directly to building design. The full-waveform calculations are important for nonlinear dynamic analysis of structures, especially long-period structures.

In this study, we did not consider nonlinear effects of soil behavior, and we only considered linear ground motions that could be expected at a bedrock level. We computed uniform hazard spectra (Figs. 11, 14, 17) and also best-fitting scenario earthquake ground motion acceleration, velocity, and displacement time histories for the three locations summarized in Table 3. We also predicted engineering parameters such as AAR, PSV, SD, and FAS based on the best-fitting scenario earthquake (Figs. 11, 14, 17). The best-fitting scenario earthquake parameters based on 2 %@50 are summarized in Table 4. Figures 12, 15, and 18 show hazard curves for different ground motion parameters such as PGA, PGV, and spectral accelerations for the periods of 0.2 s and 1 s for sites ISK, YLV, and MRM, respectively. For comparison purposes, we also computed uniform hazard spectra (Figs. 13, 16, 19) by using the classical probabilistic earthquake hazard methodology,

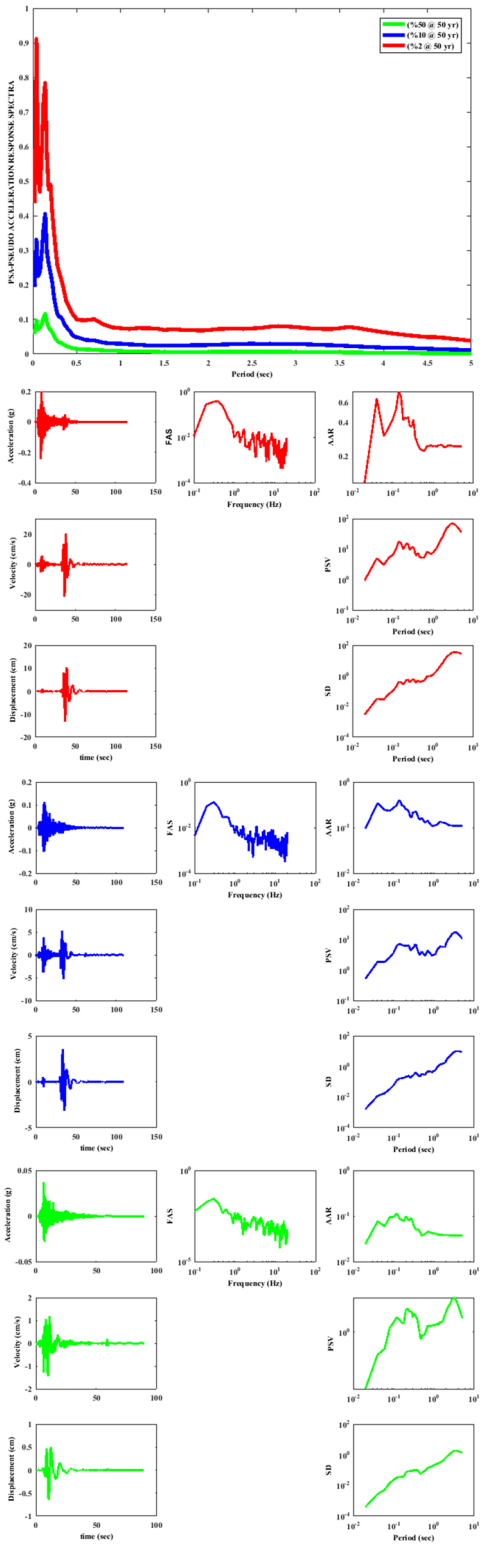

Fig. 11 Uniform hazard spectra together with best-fitted scenario earthquake time histories (ACC, VEL, DISP) and spectral parameters (FAS, AAR, PSV, SD) for station ISK (*red color* corresponds to %2@50 year, *blue* corresponds to %10@50 year, and *green* corresponds to %50@50 year)

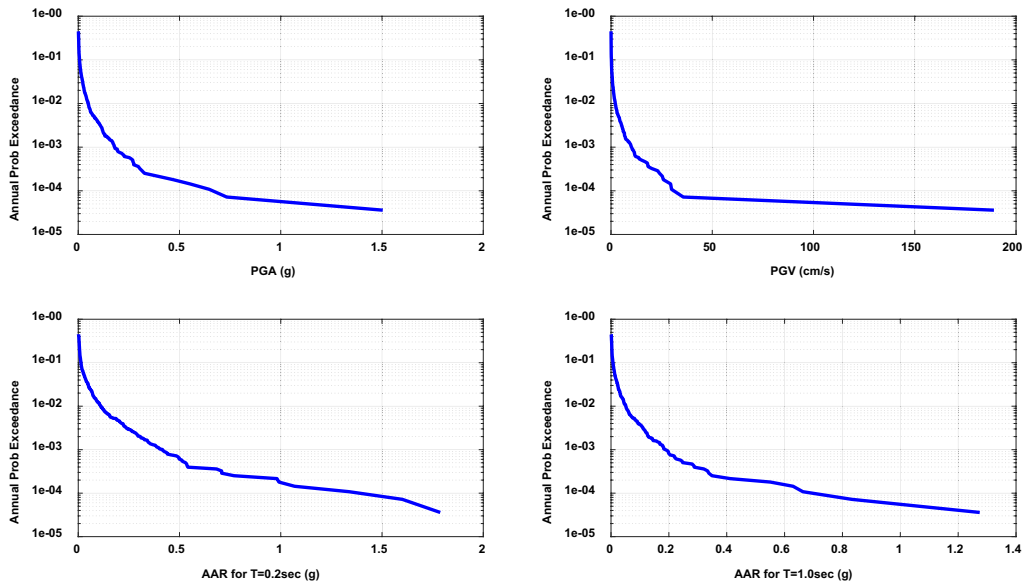

Fig. 12 Hazard curves calculated by using different ground motion parameters for station ISK

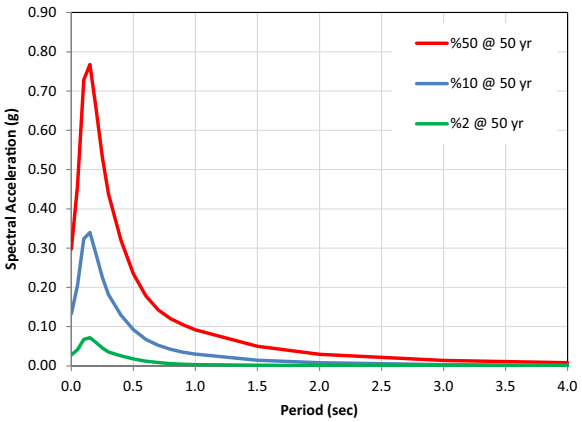

Fig. 13 Uniform hazard spectra calculated by classical PSHA for station ISK

which depends on annual probability of exceedance of an earthquake and empirical attenuation relationships, proposed by Cornell (1968). For this methodology, we used EZ-FRISK software and the same seismic sources (PIF) with the same seismicity parameters (a and b values).

We propose that our method estimated engineering parameters within a range of plus one standard deviation, and this has been validated many times by comparing to past earthquakes. As stated in Hutchings et al. (2007), "The likelihood of an earthquake falling outside the plus-and-minus standard deviation values is thus about 30 %, and the likelihood of having an earthquake above the one standard deviation value is about 15 %." The variation of both the Fourier amplitude and acceleration response spectra values for different stations is a factor of about 8 (Figs. 11, 14, 17).

If we consider recording stations with particular distances, the worldwide database for earthquakes is consistent with this factor. However, it is possible to narrow the range with additional research. Similarly, the worldwide database might show a smaller distribution if only specific faults were considered. Nevertheless, we can state that our distribution is narrow enough to be functionally useful for hazard analysis and that it is possible to reduce the uncertainty by adding more knowledge.

The results of this study can provide a basis for identifying appropriate ground motions to calculate a dynamic analysis of engineering structures and earthquake response and thus risk. After a library of seismograms is generated with broadband full-waveform synthetics, it is very easy to compile a distribution of traditional ground motion parameters, such as peak acceleration or spectral ordinates, to develop hazard curves in the form of annual probability of exceedance by using this library. Actually, by using the synthesized ground motions to achieve

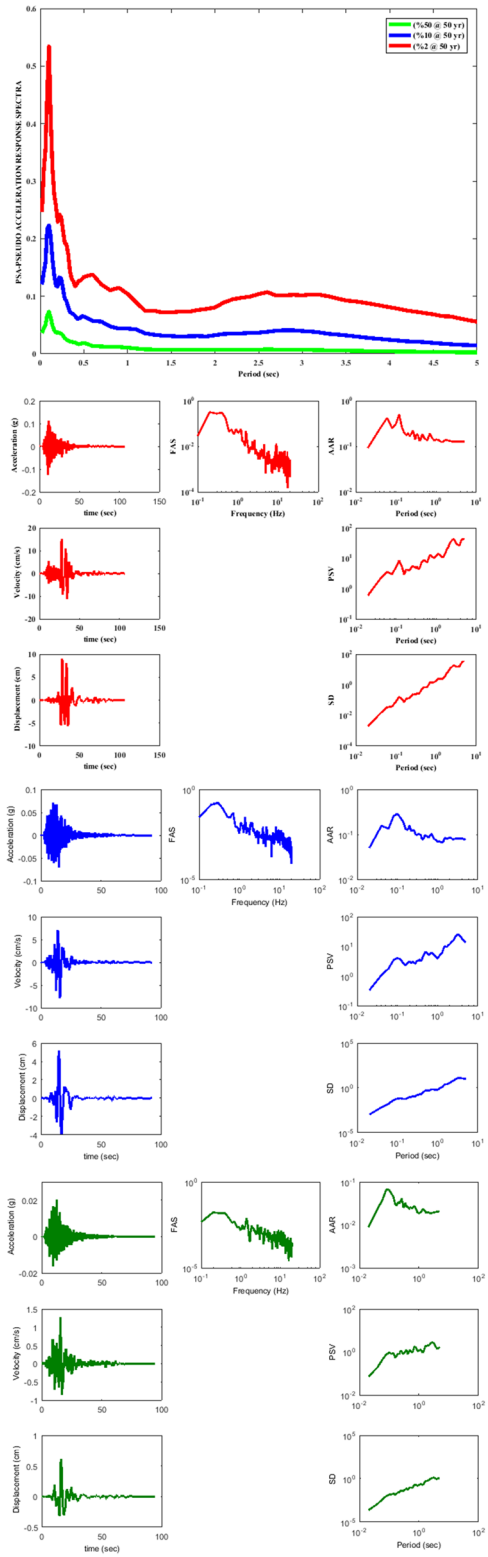

Fig. 14 Uniform hazard spectra together with best-fitted scenario earthquake time histories (ACC, VEL, DISP) and spectral parameters (FAS, AAR, PSV, SD) for station YLV. The color scheme is the same as in Fig. 9

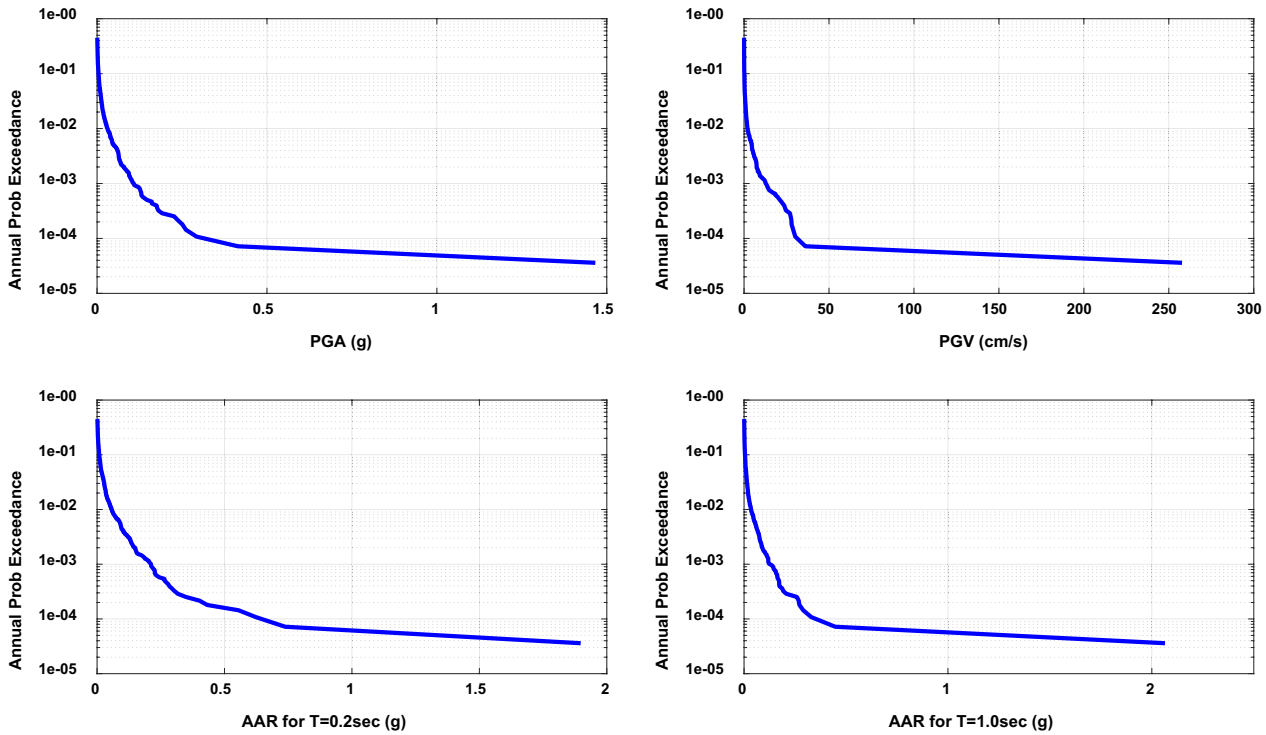

Fig. 15 Hazard curves calculated by using different ground motion parameters for station YLV

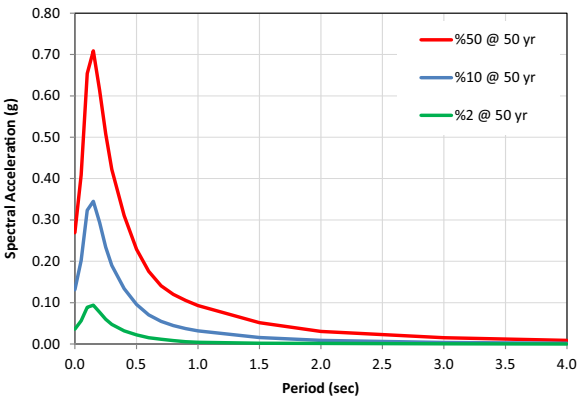

Fig. 16 Uniform hazard spectra calculated by classical PSHA for station YLV

PSHA studies with all of the requirements fulfilled, the only need is implement this procedure in a systematic way to capture the epistemic and aleatory uncertainty.

During the computation of the synthetic ground motion waveforms, we realized that there were outliers from the main distribution that represented "extreme" events. The range of this deviation was from 2 to 5 times larger than the standard deviation. On the other hand, instead of increasing with long time periods, they are replicated, so that in reality, the distributions of ground motion are naturally truncated by the physics of the earthquake cycle.

Jarpe and Kasameyer (1996) attempted to validate the same simulation procedure used in this study. To validate it, they produced broadband syntheses of the Loma Prieta earthquake at 26 sites using a simple representation of the Loma Prieta earthquake that included only moment, fault orientation, slip direction, hypocenter location, fault area, and rupture velocity. They concluded that the method produces useful time histories. One other study by Wossner et al. (2002) compared peak horizontal acceleration and response spectra in terms of spectral accelerations and peak horizontal accelerations with the attenuation laws proposed for Europe. Their results encouraged the application of the approach as a supplementary tool for site-specific ground motion prediction.

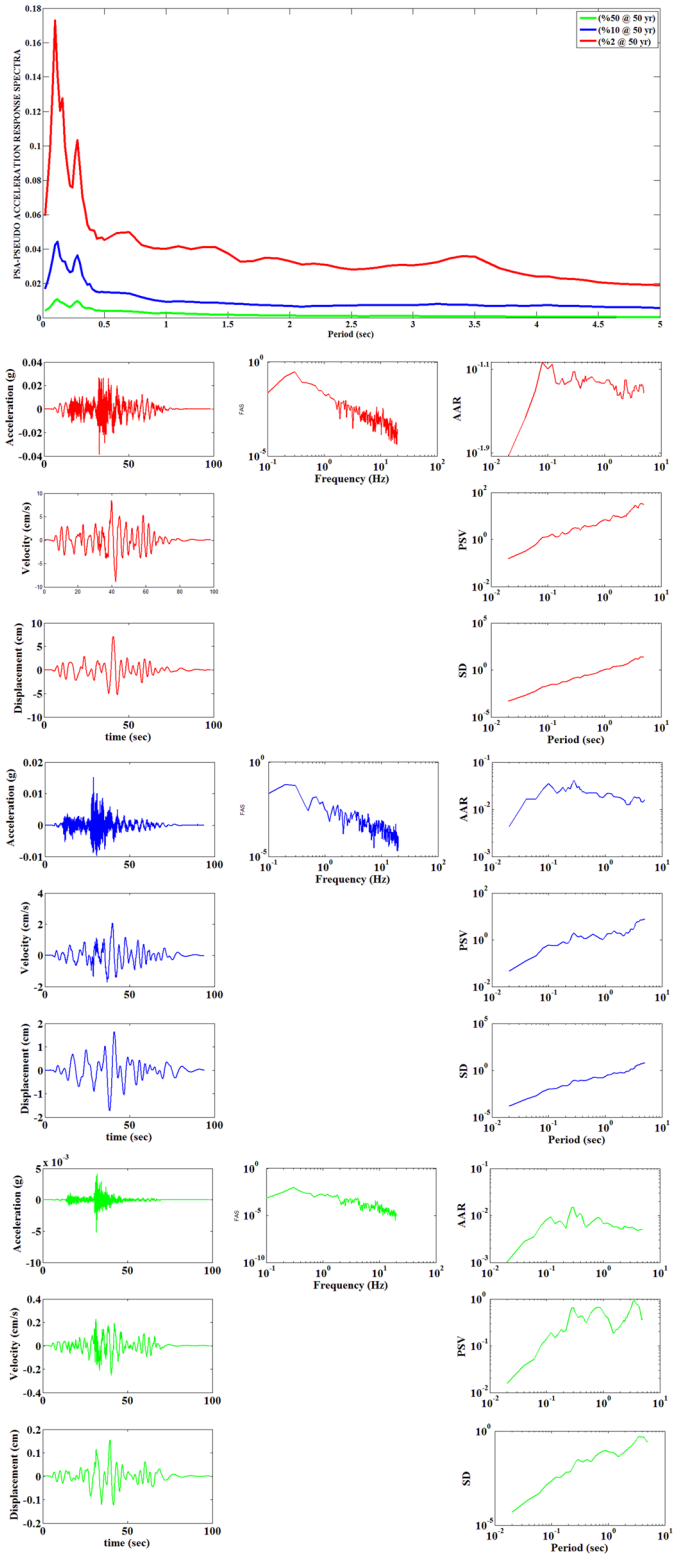

Fig. 17 Uniform hazard spectra together with best-fitted scenario earthquake time histories (ACC, VEL, DISP) and spectral parameters (FAS, AAR, PSV, SD) for station MRM. The color scheme is the same as that in Fig. 9

Table 4 Best-fitting scenario earthquake parameters based on 2 %@50

ST	SCE	PGA	PGV	Location	Moment	V_r	V_h	ROU	AM
ISK	66	0.270	18.276	N 40.894 E 28.866 14.89 km	0.354E+27	0.81	0.83	50	KH
YLV	131	0.126	19.579	N 40.838 E 29.166 10.80 km	0.647E+26	0.80	0.99	33	KK
MRM	63	0.040	6.928	N 40.780 E 29.140 4.95 km	0.372E+27	0.95	0.96	50	KK

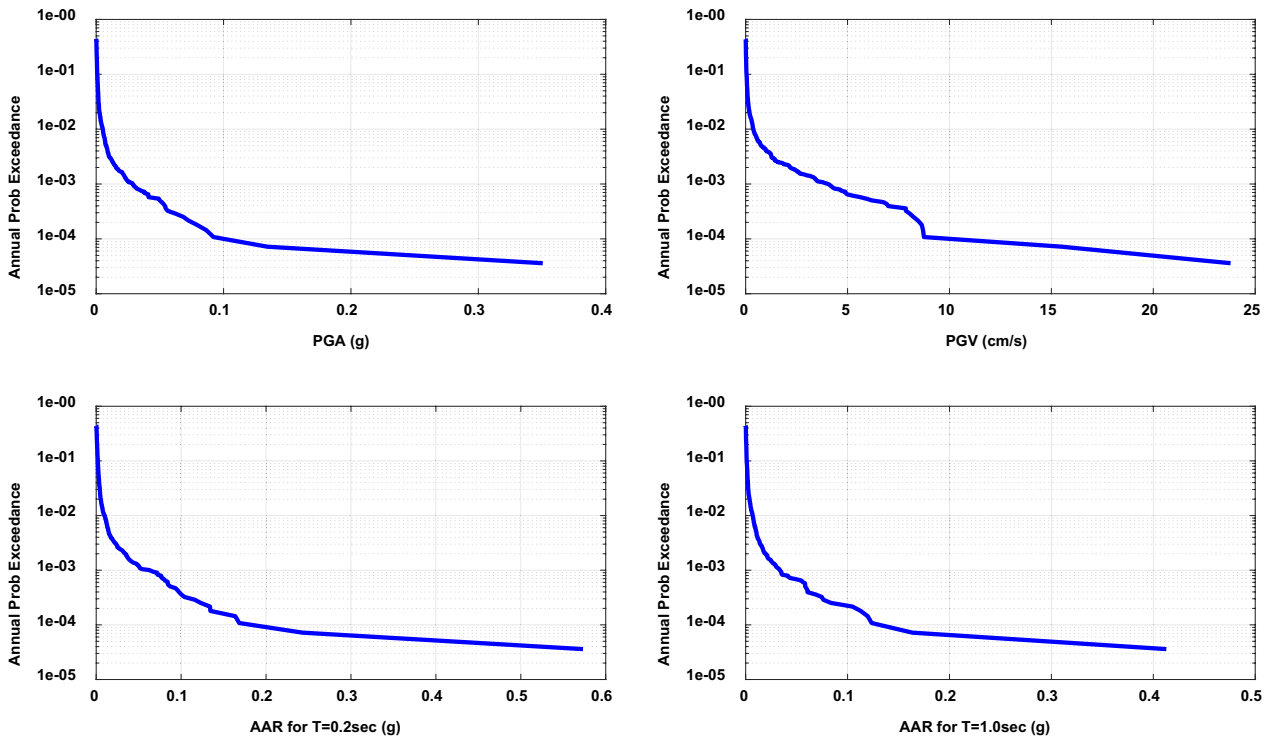

Fig. 18 Hazard curves calculated by using different ground motion parameters for station MRM

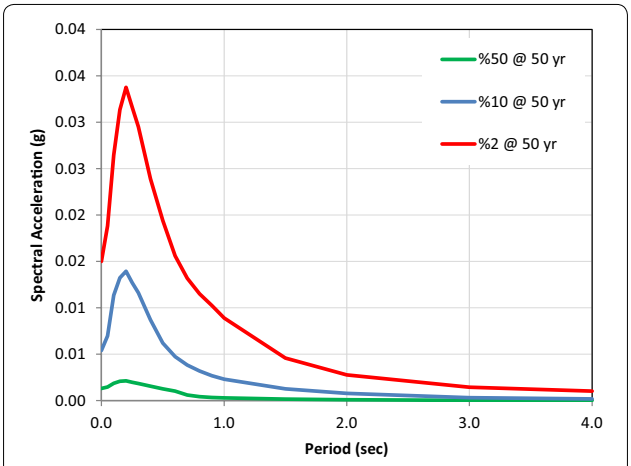

Fig. 19 Uniform hazard spectra calculated by classical PSHA for station MRM

It is important to indicate the degree of variation of the strong motion prediction calculations based on the scenario earthquake groups extracted by the Monte Carlo method. To estimate the uncertainty of a prediction of a future ground motion, we must identify the range of source parameters that could be possible for future earthquakes. A suitable range of possible source parameters is crucial for an assessment of prediction uncertainty. For this reason, we conducted a quantitative sensitivity analysis study by using different source parameters and compared these parameters with PGA and PGV. The number of source parameters that we used to assess prediction uncertainty was more than 12. We select some of these, such as moment, max asperity moment, fault duration, rise time, stress drop, average slip, rupture area, and rupture velocity, to demonstrate

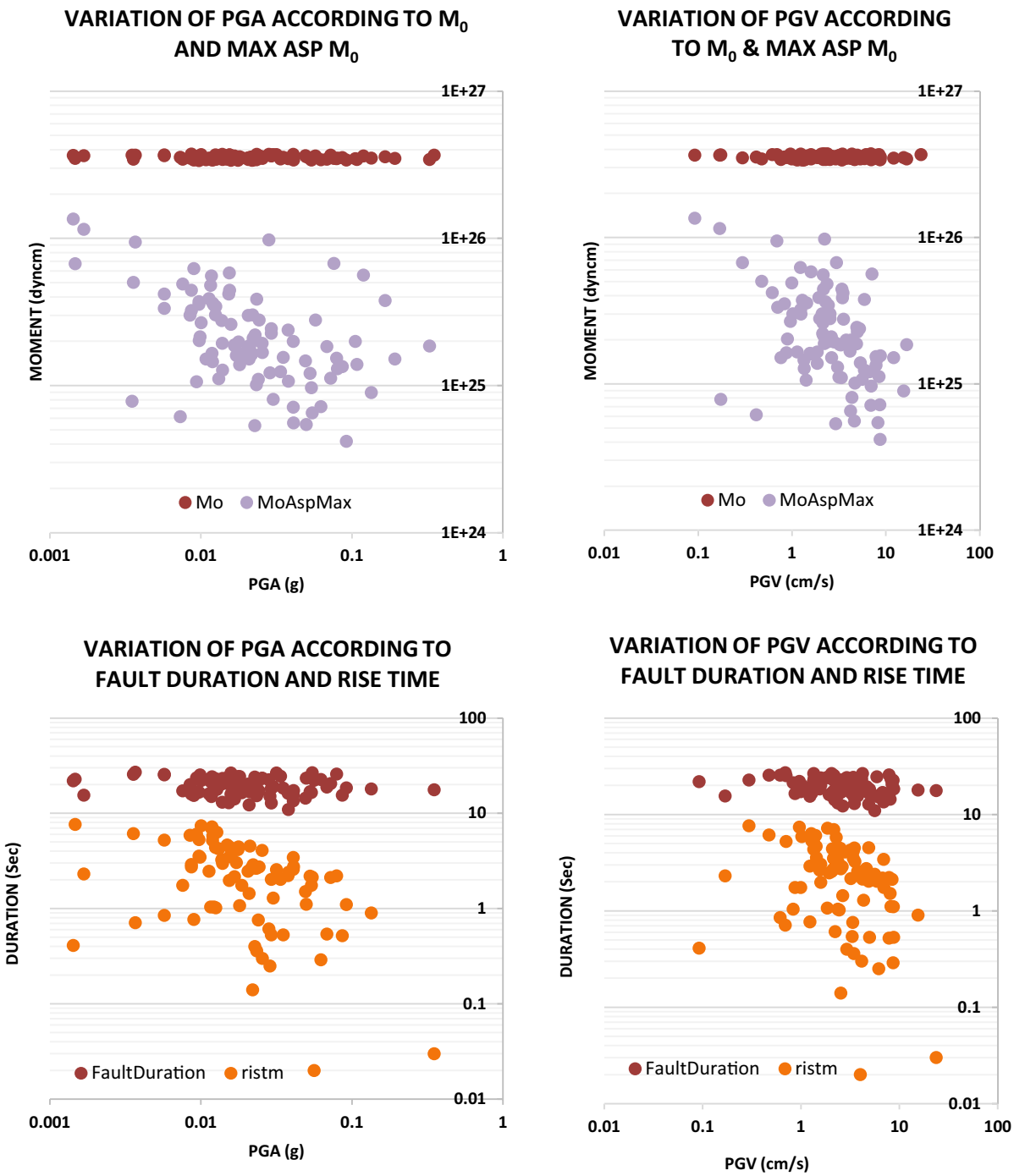

Fig. 20 Variation of moment, max asperity moment, fault duration, and rise time according to PGA and PGV. *Brown* in the *first row* is moment, and *brown* in the *second row* is fault duration

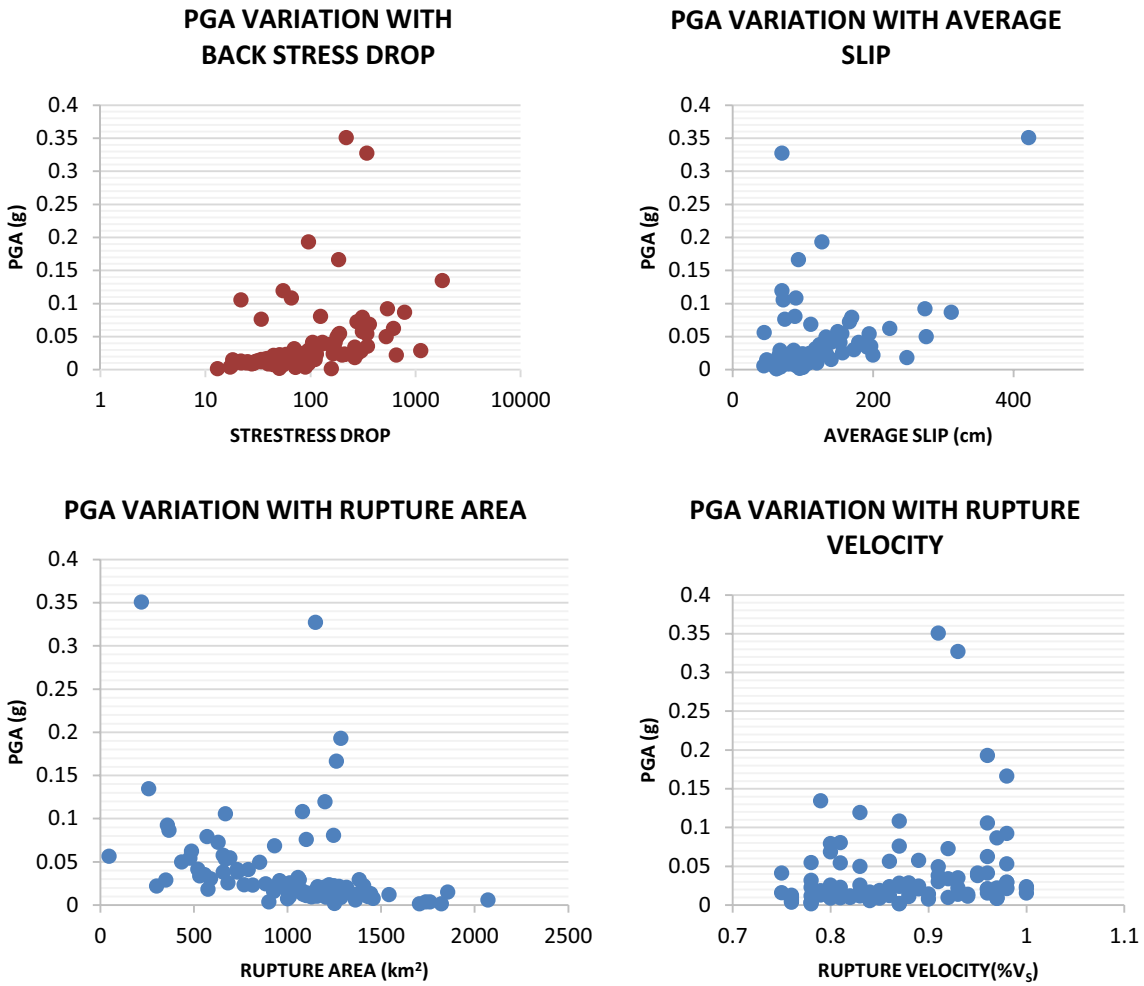

Fig. 21 Variation of back stress drop, average slip, rupture area, and rupture velocity with PGA and PGV

coherency. During the ground motion simulation process, we generated 100 different $M_w = 7$ earthquake scenarios and also used these scenarios for the sensitivity analysis. The results are presented in Figs. 20 and 21.

Abbreviations

AAR: Absolute acceleration response; BU-KOERI: Bogazici University-Kandilli Observatory and Earthquake Research Institute; BS: West Ridge; CC: Cinarcik Basin; CMF: Central Marmara Fault; EGF: Empirical Green's function; FAS: Fourier amplitude spectrum; FFT: Fast Fourier transform; GF: Green's functions; GM: Ganos Mountains; GP: Gelibolu Peninsula; KC: Kumburgaz Basin; MV: Mudurnu Valley; NAFZ: North Anatolian Fault Zone; OC: Middle Marmara Basin; PIF: Prince Island Fault; PSHA: Probabilistic seismic hazard analysis; PSV: Pseudo-spectral velocity; SD: Spectral displacement; SG: Saros Gulf; SGF: Synthetic Green's function; SSHAC: Senior Seismic Hazard Analysis Committee; TC: Tekirdag Basin.

Authors' contributions

AM carried out all types of analyses, wrote the manuscript, and plotted the figures. YMF developed and wrote subroutines to help interpret the results. LJH developed and wrote subroutines to help interpret results, wrote some parts of the manuscript, and reviewed the paper. AP helped plot the maps and provided ideas related to source parameters and rupture characteristics. All authors read and approved the manuscript.

Author details

[1] Department of Earthquake Engineering, Boğaziçi University Kandilli Observatory and Earthquake Research Institute, İstanbul, Turkey. [2] Department of Earthquake and Structural Engineering, Gebze Technical University, Kocaeli, Turkey. [3] Earth Science Division, Lawrence Berkeley National Laboratory, Berkeley, CA, USA.

Acknowledgements

This work was supported by the Boğaziçi University Research Fund Grant Number 10701 and the Scientific and Technological Research Council of Turkey (TÜBİTAK) under the 2219 Postdoctoral Research Fellowship Program, number B.14.2. TBT.0.06.01-219-84.

Competing interests

The authors declare that they have no competing interests.

Received: 3 August 2015 Accepted: 2 August 2016
Published online: 22 August 2016

References

Algermissen ST, Perkins DM, Thenhaus PC, Hanson SL, Bender BL (1982) Probabilistic estimatesof maximum acceleration and velocity in rock in the contiguous united states. U.S. Geological Survey Open-File Report 82-1033, Denver, p 99

Aki K, Richards PG (1980) Quantitative seismology theory and methods. Volumes I and II. W. H. Freeman and Company, San Francisco

Akinci A, Malagnini L, Herrmann RB, Gök R, Sorensen MB (2006) Ground motion scaling in the Marmara region, Turkey. Geophys J Int 166:635–651

Akkar S, Eroğlu AT, Çan T, Çeken U, Demircioğlu MB, Duman T, Ergintav S, Kadirioğlu FT, Kalafat D, Kale Ö, Kartal RF, Kılıç T, Özalp S, Şeşetyan K, Tekin S, Yakut A, Yılmaz AT, Zülfikar Ö (2014). Revision of Turkish Hazard Map, UDAP AFAD project, Ankara

Ambraseys NN (2001a) The earthquake of 10 July 1894 in the Gulf of Izmit (Turkey) and its relation to the earthquake of 17 August 1999. J Seismol 5:117–128. doi:10.1023/A:1009871605267

Ambraseys NN (2001b) The earthquake of 1509 in Sea of Marmara, Turkey, revisited. Bull Seismol Soc Am 91:1397–1416. doi:10.1785/0120000305

Ambraseys NN (2002a) The seismic activity of the Marmara Sea Region over the last 2000 years. Bull Seismol Soc Am 92:1–18. doi:10.1785/0120000843

Ambraseys NN (2002b) Seismic sea-waves in the Marmara Sea region during the last 20 centuries. J Seismol 6:571–578

Ambraseys NN, Finkel CF (1991) Long-term seismicity of Istanbul and of the Marmara Sea region. Terra Nova 3:527–539. doi:10.1111/j.1365-3121.1991.tb00188.x

Ambraseys NN, Jackson JA (2000) Seismicity of Sea of Marmara (Turkey) since 1500. Geophys J Int 141:F1–F6. doi:10.1046/j.1365-246x.2000.00137.x

Ansal A, Akıncı A, Cultera G, Erdik M, Pessina V, Tönük G, Ameri G (2009) Loss estimation in İstanbul based on deterministic earthquake scenarios of the Marmara Sea region (Turkey). Soil Dyn Earthq Eng 29:699–709

Armijo T, Meyer B, Navarro S, King G, Barka A (2002) Asymmetric slip partitioning in the Sea of Marmara pull-apart: a clue to propagation processes of the North Anatolian Fault? Terra Nova 14:80–86. doi:10.1046/j.1365-3121.2002.00397.x

Armijo R, Pondard N, Meyer B (2005) Submarine fault scarps in the Sea of Marmara pull-apart North Anatolian Fault: implications for seismic hazard in Istanbul. Geochem Geophys Geosyst 6(Q06009):29. doi:10.1029/2004GC000896

Atakan K, Ojeda A, Meghraoui M, Barka A, Erdik M, Bodare A (2002) Seismic hazard in Istanbul following the 17 August 1999 Izmit and 12 November 1999 Düzce earthquakes. Bull Seismol Soc Am 92:466–482

Becel A, Laigle M, Voogd B, Hirn A, Taymaz T, Galve A, Shimamura H, Murai Y, Lepine JC, Sapin M, Özalaybey S (2009) Moho, crustal architecture and deep deformation under the North Marmara trough from the SEISMARMARA Leg 1 offshore-onshore reflection-refraction survey. Tectonophysics 467:1–21

Beresnev IA, Atkinson G (1997) Modeling finite-fault radiation from the ω^n spectrum. Bull Seismol Soc Am 88:67–84

Boatwright JL (1981) Quasi-dynamic models of simple earthquake: an application to an aftershock of the 1975 Oroville, California earthquake. Bull Seismol Soc Am 71:69–94

Bohnhoof M, Bulut F, Dresen G, Malin EP, Eken T, Aktar M (2013) An earthquake gap south of Istanbul. Nat Commun. doi:10.1038/ncomms2999

Brune JN (1971) Tectonic stress and the spectra of seismic shear waves from earthquakes. J Geophys Res 75:4997–5010 **(correction, J Geophys Res 76 (20):5002, 1971)**

Caceci MS, Cacheris WP (1984) Fitting curves to data. Byte Magazine May, pp 340–360

Carton H, Singh SC, Hirn A, Bazin S, Voogd B, Vigner A, Ricolleau A, Cetin S, Ocakoğlu N, Karakoç F, Sevilgen V (2007) Seismic imaging of the three-dimensional architecture of the Çınarcık Basin along North Anatolian Fault. J Geophys Res 112:1–17

Cornell CA (1968) Engineering seismic risk analysis. Bull Seismol Soc Am 58:1583–1606

Demircioglu M (2010) Earthquake hazard and risk assessment for Turkey. PhD thesis Submitted to KOERI, Bogazici University

Durukal E, Erdik M (1994) Strong motion instrumentation of Aya Sofya and the analysis of earthquake response. In: Proceedings of the fifth US. National Conference on Earthquake Engineering, Chicago, July 10–14 1994

Emre Ö, Duman TY (2011) 1:250,000 scale active fault map series of Turkey. General Directorate of Mineral Research and Exploration, Ankara

Erdik M, Aydinoglu N, Fahjan Y, Sesetyan K, Demircioglu M, Siyahi B, Durukal E, Ozbey C, Biro Y, Akman H, Yuzugullu O (2003) Earthquake risk assessment for Istanbul metropolitan area. Earthq Eng Eng Vib 2(1):1–23

Erdik M, Demircioglu M, Sesetyan K, Durukal E, Siyahi B (2004) Earthquake hazard in Marmara region, Turkey. Soil Dyn Earthq Eng 24:605–631

Ergintav S, Reilinger RE, Çakmak R, Floyd M, Cakir Z, Dogan U, King RW, McClusky S, Özener H (2014) Istanbul's earthquake hot spots: GEODETIC constraints on strain accumulation along faults in the Marmara seismic gap. Geophys Res Lett 41:5783–5788. doi:10.1002/2014GL060985

Flerit F, Armijo R, King GCP, Meyer B, Barka A (2003) Slip partitioning in the Sea of Marmara pull-apart determined from GPS velocity vectors. Geophys J Int 154:1–7

Foxall B, Hutchings LJ, Kasameyer PW (1996) Prediction of strong ground motion based upon physical constraints on fault rupture scenarios for ground motion prediction. Lawrence Livermore National Laboratory, Livermore, CA **(UCRL-JC-11637)**

Gardner JK, Knopoff L (1974) Is the sequence of earthquakes in Southern California, with aftershocks removed, Poissonian? Bull Seismol Soc Am 64:1363–1367

Gök R, Hutchings L, Mayeda K, Kalafat D (2009) Source parameters for 1999 North Anatolian Fault Zone aftershocks. Pure appl Geophys. doi:10.1007/s00024-009-0461-x

Golara A, Jazany RA (2013) An improvement on the use of empirical Green functions for ground motion synthesis to predict Tehran's main earthquake. International Institute of Earthquake Engineering and Seismology (IIEES), Structural Research Centre, Tehran, Iran. Sci Res Essays 8(19):731–753

Görür N, Çağatay MN, Sakinç M, Sümengen M, Şentürk K, Yaltirak C, Tchapalyga A (1997) Origin of the Sea of Maramara as deduced from Neogene to Quaternary paleogeographic evolution of its frame. Int Geol Rev 39:342–352

Graves RW, Pitarka A (2004) Broadband time history simulations using a hybrid approach. Paper presented at the 13th World Conference Earthquake Engineering, Vancouver, Canada, 1–6 August 2004

Grünthal G, Wahlström R (2012) The European-Mediterranean Earthquake Catalogue (EMEC) for the last millennium. J Seismol 16(3):535–570. doi:10.1007/s10950-012-9302-y

Gürbüz C, Aktar M, Eyidoğan H, Cisternas A, Haessler H, Barka A, Ergin M, Türkelli N, Polat O, Üçer B, Kuleli S, Baris S, Kaypak B, Bekler T, Zor E, Biçmen F, Yörük A (2000) The seismotectonics of the Marmara Region (Turkey): results from a microseismic experiment. Tectonophysics 316:1–17

Hanks TC, Kanamori H (1979) A moment magnitude scale. J Geophys Res 84(B5):1348–2350

Hartzell SS, Harmsen A, Frankel A, Larsen S (1999) Calculation of broadband time histories of ground motion: comparison of methods and validation using strong ground motion from the 1994 Northridge earthquake. Bull Seismol Soc Am 89:1484–1504

Hergert T, Heidbach O, Becel A, Laigle M (2011) Geomechanical model of the Marmara Sea region–I. 3-D contemporary kinematics. Geophys J Int 185:1073–1089. doi:10.1111/j.1365-246X.2011.04991.x

Heuze FE, Ueng TS, Hutchings LJ, Jarpe SP, Kasameyer PW (1994) A coupled seismic-geotechnical approach to site-specific strong motion. Soil Dynamics and Earthquake Engineering 16(4):259–271

Hubert-Ferrari A, Barka A, Jacques E, Nalbant SS, Meyer B, Armijo R (2000) Seismic hazard following the 17 August 1999 Izmit earthquake. Nature 404:269–273. doi:10.1038/35005054

Hutchings L (1991) "Prediction" of strong ground motion for the 1989 Loma Prieta earthquake using empirical Green's functions. Bull Seismol Soc Am 81:88–121

Hutchings LJ (1994) Kinematic earthquake models and synthesized ground motion using empirical Green's functions. Bull Seismol Soc Am 84:1028–1050

Hutchings L (2001) Program NetMoment, a simultaneous inversion for moment, source corner frequency, and site specific t^*. Lawrence Livermore National Laboratory, Livermore, CA **(UCRL-ID 135693)**

Hutchings LJ (2006) Program HAZARD, Generate different earthquake scenarios using by Monte Carlo algorithm, Lawrence Berkeley National Laboratory, Livermore, CA

Hutchings L, Wu F (1990) Empirical Green's functions from small earthquakes: a waveform study of locally recorded aftershocks of the San Fernando earthquake. J Geophys Res 95:1187–1214
Hutchings LJ, Jarpe S (1996) Ground-motion variability at the Highway 14 and I-5 interchange in the northern San Fernando Valley. Bull Seismol Soc Am 86:289–299
Hutchings LJ, Kasameyer PW, Jarpe SP, William F (1997) Synthetic strong ground motions for a magnitide 7.25 hayward fault earthquake. Lawrence Livermore National Laboratory, Livermore, CA **(UCRL-CR-1232201)**
Hutchings L, Jarpe S, Kasameyer P (1998) Validation of a ground motion synthesis and prediction methodology for the 1988, M = 6.0, Saguenay Earthquake. Lawrence Livermore National Laboratory, Livermore, CA **(UCRL-JC-129395)**
Hutchings L, Ioannidou E, Kalogeras I, Voulgaris N, Savy J, Foxall W, Scognamiglio L, Stavrakakis G (2007) A physically-based strong ground-motion prediction methodology; application to PSHA and the 1999 M = 6.0 Athens earthquake. Geophys J Int 168:569–680
Irikura K (1986) Prediction of strong acceleration motions using empirical Green's function. In: Proceedings of the 7th Japan conference on earthquake engineering
Irikura K, Kamae K (1994) Estimation of strong ground motion in broad-frequency band based on a seismic source scaling model and an empirical Green's function technique. Ann Geofis 37:1721–1743
Jarpe SJ, Kasameyer PK (1996) Validation of a methodology for predicting broadband strong motion time histories using kinematic rupture models and empirical Green's functions. Bull Seismol Soc Am 86:1116–1129
Kalafat D, Gunes Y, Kekovalı K, Kara M, Deniz P, Yilmazer M (2011) Bütünleştirilmiş homojen deprem kataloğu (1900-2010;M $\geq$ 4.0). B.Ü. Kandilli Rasathanesi ve Deprem Arş. Enst
Kamae K, Irikura K, Piturka A (1998) A technique for simulating strong ground motion using hybrid Green's function. Bull Seismol Soc Am 88:357–367
Karabulut H, Özalaybey S, Taymaz T, Aktar M, Selvi O (2003) Kocaoğlu A (2003) A tomographic image of the shallow crustal structure in the eastern Marmara. Geophys Res Lett 30(24):2777. doi:10.1029/2003GL018074
Kurtuluş C, Canbay MM (2007) Tracing the middle strand of the North Anatolian Fault Zone through the southern Sea of Marmara based on seismic reflection studies. Geo-Mar Lett 27:27–40
Laigle M, Becel A, Voogd B, Hirn A, Taymaz T, Ozalaybey S (2008) A first deep seismic survey in the sea of Marmara: deep basins and whole crust architecture and evolution. Earth Planet Sci Lett 270:168–179
Lama RD, Vutukuri VS (1978) Handbook on mechanical properties of rocks. V II, R.D. Trans Tech Publications, pp 245–481
Larsen S (1995) E3D: 2D/3D elastic finite-difference wave propagation code
Le Pichon X, Sengör AMC, Demirbag E, Rangin C, Imren C, Armijo R, Görür N, Cagatay N, Mercier De Lepinay B, Meyer B, Saatcilar R, Tok B (2001) The active main Marmara fault. Earth Planet Sci Lett 192:595–616
Liu P, Archuleta RJ, Hurtzell SH (2006) Prediction of broadband ground-motion time histories: hybrid low-frequency method with correlated random source parameters. Bull Seismol Soc Am 96:2118–2130. doi:10.1785/0120060036
Mai PM, Imperatori W, Olsen BK (2010) Hybrid broadband ground-motion simulations: combining long-period deterministic synthetics with frequency multiple S-to-S backscattering. Bull Seismol Soc Am 100(5A):2124–2142
McCallen D, Larsen S (2003) NEVADA—a simulation environment for regional estimation of ground motion and structural response. A final report for the Laboratory directed research and development project 02-ERD-044 UCRL
Meade BJ, Hager BH, Mcclusky SC, Reilinger RE, Ergintav S, Lenk O (2002) Estimates of seismic potential in the Marmara Sea Region from block models of secular deformation constrained by global positioning system measurements. Bull Seismol Soc Am 92:208–215. doi:10.1785/0120000837
Mena BE, Durukal E, Erdik M (2006) Effectiveness of hybrid Green's function method in the simulation of near-field strong notion: an application to the 2004 Parkfield earthquake. Bull Seismol Soc Am 100(5A):2143–2162
Mert A, Fahjan Y, Pinar A, Hutchings L (2014a) Prens adaları fayında kuvvetli yer hareketi benzesimleri. IMO Teknik Dergi 419:6775–6804
Mert A, Fahjan Y, Pinar A, Hutchings L (2014b) Marmara Bölgesinde Ampirik Green Fonksiyon Yöntemiyle Deprem Benzeşimlerinin Elde Edilmesi. Hacettepe Universitesi Yerbilimleri Uygulama ve Araştırma Merkezi Bulteni, Yerbilimleri 35(1):55–78
Nalbant SS, Hubert A, King GCP (1998) Stress coupling between earthquakes in northwest Turkey and the north Aegean Sea. J Geophys Res 103:24469–24486. doi:10.1029/98JB01491
Nelder JA, Mead R (1965) A simplex method for function minimization. Comput J 7:308
Nicknam A, Eslamian Y (2011) An EGF-based methodology for predicting compatible seismograms in the spectral domain using GA technique. Geophys J Int 185:557–583
Oncel OA, Alptekin O (1999) Effect of aftershocks on earthquake hazard estimation: an example from the North Anatolian Fault Zone. Nat Hazards 19:1–11
Oncel OA, Wilson T (2006) Evaluation of earthquake potential along the Northern Anatolian Fault Zone in the Marmara Sea using comparisons of GPS strain and seismotectonic parameters. Tectonophysics 418:205–218
Oncel OA, Wyss M (2001) The major asperities of the 1999 Mw = 7.4 Izmit earthquake defined by the microseismicity of the two decades before it. Geophys J Int 143:501–506
Örgulu G (2011) Seismicity and source parameters for small-scale earthquakes along the splays of the North Anatolian Fault (NAF) in the Marmara Sea. Geophys J Int 184:385–404
Papoulia J, Fahjan YM, Hutchings L, Novikova T (2015) PSHA for broad-band strong ground-motion hazards in the Saronikos Gulf, Greece, from potential earthquake with synthetic ground motion. J Earthq Eng 19:624–648
Parsons T (2004) Recalculated probability of M 7 earthquakes beneath the Sea of Marmara Turkey. J Geophys Res 109:B05304. doi:10.1029/2003JB002667
Parsons T, Toda S, Stein RS, Barka A, Dieterich JH (2000) Heightened odds of large earthquakes near Istanbul: an interaction-based probability calculation. Science 288:661–665. doi:10.1126/science.288.5466.661
Pinar A, Kuge K, Honkura Y (2003) Moment inversion of recent small to moderate sized earthquakes: implications for seismic hazard and active tectonics beneath the Sea of Marmara. Geophys J Int 153:133–145. doi:10.1046/j.1365-246X.2003.01897.x
Pitarka A, Somerville P, Fukushima Y, Uetake T, Irikura K (2000) Simulation of near fault strong ground motion using hybrid Green's functions. Bull Seismol Soc Am 90:566–586
Pondard N, Armijo R, King GCP, Meyer B, Flerit F (2007) Fault interactions in the Sea of Marmara pullapart (North Anatolian Fault): earthquake clustering and propagating earthquake sequences. Geophys J Int 171(3):1185. doi:10.1111/j.1365-246X.2007.03580.x
Prejean SG, Ellsworth WL (2001) Observations of earthquake source parameters and attenuation at 2 km depth in the Long Valley Caldera, eastern California. Bull Seismol Soc Am 91:165–177
Pulido N, Kubo T (2004) Near-fault strong-motion complexity of the 2000 Tottori earthquake (Japan) from a broadband asperity model. Tectonophysics 390:177–192
Pulido N, Matsuoka M (2006) Broadband strong motion simulation of the 2004 Niigata-ken Chuetsu earthquake: Source and site effects. Third international symposium on the effects of surface geology on seismic motion, Grenoble, France, vol 1, pp 657–666
Pulido N, Ojeda A, Atakan K, Kubo T (2004) Strong ground motion estimation in the Sea of Marmara region (Turkey) based on a scenario earthquake. Tectonophysics 391:357–374
Rodgers A, Petersson NA, Nilsson S, Sjogreen B, McCandless K (2008) Broadband waveform modelling of moderate earthquakes in San Francisco Bay area and preliminary assessment of the USGS 3D seismic velocity model. Bull Seismol Soc Am 98:969–988
Rosset PH, Wagner J-J, Garcia-Fernandez M, Jimenez MJ (1998) Strong ground motion simulation with empirical green's functions; first attempts in the framework of the European Project SERGISAI. EC Environment Research Programme, Climatology and Natural Hazards (1994–1998)
Sato T, Kasahara J, Taymaz T, Ito M, Kamimura A, Hayakawa T, Tan O (2004) A study of microearthquake seismicity and focal mechanisms within the sea of Marmara (NW Turkey) using ocean bottom seismometers (OBSs). Tectonophysics 391:303–314
Schulz CH (2002) The mechanics of earthquakes and faulting. Cambridge University Press, Cambridge, p 471
Scognamiglio L, Hutchings L (2009) A test of a physically-based strong ground motion prediction methodology with the 27 September 1997, M_w = 6.0 Colfiorito (Umbria-Marcha sequence), Italy earthquake. Tectonophysics 476:145–158

Somerville P, Irikura K, Graves R, Sawada S, Wald D, Abrahamson N, Iwasaki Y, Kagawa T, Smith N, Kowada A (1999) Characterizing crustal earthquake slip models for the prediction of strong ground motion. Seismol Res Lett 70(1):59–80. doi:10.1785/gssrl.70.1.59

Sørensen BM, Pulido N, Atakan K (2007) Sensitivity of ground-motion simulations to earthquake source parameters: a case study for Istanbul, Turkey. Bull Seismol Soc Am 97(3):881–900

SSHAC (Senior Seismic Hazard Committee) (1997) Recommendations for Probabilistic Seismic Hazard Analysis: Guideline on Uncertainty and Use of Experts, US Nuclear Regulatory Commission Report CR-6372, Washington DC

Stein RS, Barka AA, Dieterich JH (1997) Progressive failure on the North Anatolian Fault since 1939 by earthquake stress triggering. Geophys J Int 128:594–604. doi:10.1111/j.1365-246X.1997.tb05321.x

Tanircan G (2012) İstanbul için 3 boyutlu hız modeli ile yer hareketi simülasyonu. Gazi Üniversitesi Mühendislik Mimarlık Fakültesi Dergisi. 27(1):27–35

Toksöz MN, Relinger RE, Doll CG, Barka AA, Yalçin N (1999) Izmit (Turkey) earthquake of 17 August 1999: first report. Seismol Res Lett 70:669–679

Ustaomer T, Gokasan E, Tur H, Gorum T, Batuk F, Kalafat D, Alp H, Ecevitoglu B, Birkan H (2008) Faulting, mass-wasting and deposition in an active dextral shear zone, the Gulf of Saros and the NE Aegean Sea, NW Turkey. Geo-Mar Lett 28:171–193. doi:10.1007/s00367-007-0099-6

Wells DL, Coppersmith KJ (1994) New empirical relationship among magnitude, rupture length, rupture width, rupture area and surface displacement. Bull Seismol Soc Am 84(4):974–1002

Wiemer S, Wyss M (2000) Minimum magnitude of completeness in earthquake catalogs: examples from Alaska, the western United States, and Japan. Bull Seismol Soc Am 90(4):859–869

Wossner J, Treml M, Wenzel F (2002) Simulation of $M_w = 6.0$ earthquakes in the Upper Rhine graben using empirical Green functions. Geophys J Int 151:487–500

Yilmaz Y, Gökaşan E, Erbay AA (2009) Morphotectonic development of the Marmara Region. Tectonophysics. doi:10.1016/j.tecto.2009.05.012